Precambrian Research 413 (2024) 107573

Contents lists available at ScienceDirect

Precambrian Research

journal homepage: www.elsevier.com/locate/precamres

The potential for reconstructing primary ocean chemistry from hypogene and supergene altered banded iron formations: An example from Weld Range, Western Australia

Samantha C. Russo[a,b,*], Alex J. McCoy-West[a,b], Paul Duuring[c]

[a] IsoTropics Geochemistry Laboratory, Earth and Environmental Science, James Cook University, Townsville, Queensland 4811, Australia
[b] Economic Geology Research Centre, James Cook University, Townsville, Queensland 4811, Australia
[c] Geological Survey of Western Australia, Department of Energy, Mines, Industry Regulation and Safety, Perth, Western Australia 6004, Australia

ARTICLE INFO

Keywords:
Banded iron formation
Paleo-environmental reconstruction
Seawater
Sequential extraction
Hypogene and supergene alteration
Rare earth elements

ABSTRACT

Pristine banded iron formations (BIF) are established paleo-environmental proxies for reconstructing the elemental and isotopic signatures of the ancient seawater that they precipitated from. Negligible changes in shale-normalised rare earth element patterns in BIF throughout Earth's history, including features such as low La/Yb ratios, and positive La, Eu, Gd, and Y anomalies, and near- to super-chondritic Y/Ho ratios support the preservation of ancient seawater signatures. Nevertheless, limiting paleo-environmental reconstructions to pristine BIF imparts a significant sampling bias and restricts understanding of the temporal evolution of the oceans. However, altered BIF samples are problematic for paleo-environmental reconstructions due to the risk of disturbance of their primary signatures. Instead, mineral-/fraction-specific analysis potentially provides robust paleo-environmental reconstructions where primary mineral phases are preserved, with the three main mineral fractions in pristine and altered BIF including carbonates (e.g., siderite and ankerite), Fe oxides (e.g., magnetite, hematite, and goethite), and silicates (e.g., quartz and Fe-silicates). This study investigates samples from the ca. 2.7 Ga Weld Range BIF, located in the Youanmi Terrane, Yilgarn Craton, Western Australia. The lower-greenschist facies BIF varies from least-altered to progressively hypogene- and/or supergene-altered. Whole-rock analysis of these rocks revealed the preservation of seawater-like signatures despite significant alteration, such as positive La, Eu and Y anomalies. Additionally, sequential extraction techniques were performed on the least-altered and altered BIF samples to separately analyse the carbonate, Fe oxide, and silicate mineral fractions. In both the least- and hypogene-altered samples all fractions preserved evidence for seawater-like chemistry despite extensive precipitation of secondary hypogene carbonate and Fe oxide minerals in the latter. The seawater-like characteristics preserved in the hypogene carbonate and Fe oxide-fractions are the result of the seawater-magmatic fluid mixture that precipitated hypogene replacement minerals. Therefore, we interpret the silicate-fraction to be the most indicative of the primary seawater that precipitated the Weld Range BIF, where the quartz/chert reflects amorphous silica signatures that are unaffected by low-grade metamorphism and hypogene alteration. The preservation of primary mineral phases (i.e., silicates) and characteristic seawater signatures in the extensively altered Weld Range BIF, suggests that altered BIF should be more widely investigated to improve the breadth and representativeness of global paleo-environmental reconstructions.

1. Introduction

The elemental and isotopic signatures of chemical sediments, such as banded iron formations (BIF), are used as paleo-environmental proxies to understand the chemical and physical conditions of our oceans through geologic time (e.g., Bau, 1993; Bau and Dulski, 1999; Ernst and Bau, 2021; Planavsky et al., 2010). Numerous studies have demonstrated that shale-normalised rare earth element (REE) patterns in BIF are similar to shale-normalised REE patterns in modern seawater, and can therefore be used as a proxy for primary ancient seawater due to

---

* Corresponding author at: IsoTropics Geochemistry Laboratory, Earth and Environmental Science, James Cook University, Townsville, Queensland 4811, Australia.
E-mail address: samantha.russo@my.jcu.edu.au (S.C. Russo).

https://doi.org/10.1016/j.precamres.2024.107573
Received 30 December 2023; Received in revised form 31 July 2024; Accepted 18 September 2024

insignificant changes in REE seawater signatures through time (Alexander et al., 2009; Alibert, 2016; Alibert and McCulloch, 1993; Bau, 1993; Bau and Dulski, 1996; Bolhar et al., 2004; Bolhar et al., 2005a; Ernst and Bau, 2021; Haugaard et al., 2016; Konhauser et al., 2017a; Oonk et al., 2018; Planavsky et al., 2010). However, a limitation of paleo-environmental reconstruction studies, particularly for the Archean, is a potential sampling bias. For ancient samples there is a significant and unavoidable sampling bias related to incomplete preservation of continental crust, which is further compounded by the greater likelihood of secondary alteration over time. Thus, examining only pristine/least-altered BIF samples results in a highly restricted pool of suitable samples and therefore potentially compromises the representativeness of any proxy record. The alternative approach of using altered BIF samples for paleo-environmental reconstructions, such as those altered by hypogene and/or supergene processes, has been cautioned due to the risk of overprinting primary signatures by alteration fluids, especially where an open-system is observed (Basu et al., 2022; Bau, 1993; Bonnand et al., 2020; Gong et al., 2021; Ingalls and Snell, 2021; Li et al., 2021; Nan et al., 2023; Stammeier et al., 2019). Nevertheless, elemental mobility is dependent on water/rock ratios, dissolution of primary minerals, formation of secondary minerals, the physico-chemical environment, and the composition of the alteration fluid/s (Alexander et al., 2008; Bau, 1991; Bau, 1993; Migdisov et al., 2016). Therefore, if the mineralogy of altered samples is properly understood and remnant primary phases are present, these samples could be carefully analysed for paleo-environmental reconstruction purposes. In this study, we undertook a series of whole-rock and fraction-specific geochemical analyses on least-, hypogene- and/or supergene-altered BIF samples from ca. 2.7 Ga Weld Range BIF, Yilgarn Craton, Western Australia to understand the potential of undertaking paleo-environmental reconstructions in altered Archean BIF.

2. Suitability of different mineral fractions in pristine and altered BIF as paleo-environmental proxies

Pristine and altered BIF comprises three major mineralogical fractions; Fe oxides (e.g., magnetite, hematite, and goethite), silicates (e.g., chert/quartz and Fe-silicates) and carbonates (e.g., siderite, ankerite, calcite, and dolomite). The exact formation mechanisms, including the precipitation and diagenetic pathways of these minerals remain debated (Ernst and Bau, 2021; Ghosh, 2020; Rasmussen et al., 2013; Rasmussen et al., 2017). However, their deposition (particularly Fe oxides and silicates) is controlled by episodic hydrothermal events dominating the oceanic budget, as well as current upwelling, redox, pH and temperature (Ghosh, 2020; Hamade et al., 2003; Haugaard et al., 2016; Planavsky et al., 2010; Thompson et al., 2019). Regarding episodic hydrothermal events, Ghosh (2020) suggests that during these events Fe-silicates are formed by instantaneous coprecipitation of hydrothermally delivered Fe^{2+} and silica (in the form of $Si(OH)_4$), which was enriched in the Archean oceans. Once the hydrothermal event has ceased, and Fe-silicate formation continues, eventually resulting in the depletion of the Fe^{2+} reservoir, then silica precipitation begins to dominate. In the Archean oceans, silica precipitation was facilitated by polymerisation in shallow oceanic settings, by evaporative concentration (Cloud, 1973; Currie and Perry, 2008; Drever, 1974; Fischer and Knoll, 2009; Morris, 1993). When the silica reservoir becomes exhausted, the Fe^{2+} reservoir accumulates from successive hydrothermal events, with the Fe^{2+} oxidising to Fe^{3+} and later transforming into Fe oxides that are preserved in BIF (Hamade et al., 2003; Morris, 1993). Different Fe^{2+} oxidative pathways of Fe oxides have been suggested before and following the Great Oxidation Event (GOE; ca.2.4 Ga; Gumsley et al., 2017). Pre-GOE, oxidation of Fe^{2+} was largely facilitated by anoxygenic photosynthesis (i.e., photoferrotrophs; Garrels et al., 1973; Hartman, 1984; Konhauser et al., 2017b; Walter et al., 2014), whereas post-GOE, oxidation was dominated by oxygenic photosynthesis (Fischer et al., 2016; Ozaki et al., 2019; Wang et al., 2023). Photocatalytic oxidation is another plausible precipitation pathway of Fe oxides pre-GOE where oxidation is achieved via adsorption of ultraviolet light due to the lack of an ozone layer (Cairns-Smith, 1978; Konhauser et al., 2007; Tabata et al., 2021). However, it is unlikely that this pathway would have resulted in large scale accumulations of Fe oxides (Konhauser et al., 2007). Similarly, post-depositional diagenesis of Fe silicates can also facilitate the separation and precipitation of alternating Fe- and Si-rich bands (Rasmussen et al., 2013; Rasmussen et al., 2019; Rasmussen et al., 2017), however, this is unlikely to be major precipitation pathway of Fe oxides and silicates in BIF (Bau and Alexander, 2009; Bau and Dulski, 1992; Ernst and Bau, 2021).

As for carbonates in BIF, these are divided into Fe-rich carbonates (i.e., siderite and ankerite) and Ca-Mg carbonates (i.e., calcite and dolomite). Precipitation of Fe-rich carbonates are attributed to reactions between Fe^{2+} and bicarbonate ions in seawater, diagenesis or through dissimilatory iron reduction (Beukes et al., 1990; Johnson et al., 2008; Köhler et al., 2013; Winter and Knauth, 1992). On the other hand, Ca-Mg carbonate deposition was likely controlled by the CO_2 partial pressure in the ocean (Holland, 1965) and/or encouraged by photosynthetic algae at the surface (Cameron and Baumann, 1972; Schopf and Barghoorn Elso, 1967). Many unknowns of Ca-Mg carbonate deposition persist due to its scarcity in the Archean rock record. Nevertheless, the robustness of each mineralogical fraction for paleo-environmental reconstructions of ancient seawater chemistry is briefly discussed below.

The robustness of BIF for paleo-environmental reconstructions hinges on the negligible fractionation of elements, namely REE, during adsorption and coprecipitation onto BIF minerals (i.e., Fe oxides, silicates, and carbonates). For example, fractionation of REE onto Fe-(oxy) hydroxides (a precursor mineral for Fe oxides) is considered negligible in the Archean oceans due to low concentrations of CO_3^{2-} (where high concentrations would retain HREE in solution), high partition coefficients (e.g., log $K_d = > 3$–4) and high Fe/REE ratios (e.g., 10^5-10^6; Alibert, 2016; Bau and Möller, 1993; Cloud, 1973; Liu et al., 2017; Quinn, 2006). Similarly, mechanisms, such as high partition coefficients (log $K_d > 1$), are also observed during the uptake of transition metals onto Fe-(oxy)hydroxides, indicating negligible fractionation (Takematsu, 1979). Therefore, elemental concentrations of Fe oxides in BIF are considered representative and proportionate to the seawater that they precipitated from.

As for silicate phases, fractionation of elements during precipitation of Fe-silicates is considered highly unlikely due to the instantaneous coprecipitation of Fe and Si from the Archean ocean (Ghosh, 2020), whereas silica has been expressed to have a higher affinity for elements with smaller radii (i.e., a higher affinity for HREE relative to LREE, Alibert, 2016; Barany and Strelko, 2013; Takahashi et al., 2006). Despite this, Viehmann et al. (2020) demonstrated that well-preserved cherts from the Strelley Pool Formation, Western Australia, preserved seawater-like compositions. Comparable to the Fe oxides, very large Si/elemental ratios may have resulted in proportional uptake of elements from seawater. These elemental signatures remain unfractionated during post-depositional processes (e.g., diagenesis and/or low-grade metamorphism), suggesting that these samples are suitable for paleo-environmental reconstructions (Bau, 1991; Bau, 1993; Bau and Dulski, 1992; McConchie, 1987).

Carbonate minerals within BIF have also been proposed to preserve seawater signatures, particularly Ca-Mg carbonates due to possible microbial diagenesis effects in Fe-rich carbonates (Heimann et al., 2010; Johnson et al., 2013). Coprecipitation of carbonate and REE is easily achieved due to similar radius size between REE^{3+} and Ca^{2+} (Smrzka et al., 2019; Zhong and Mucci, 1995). However, fractionation of REE in carbonates can occur where strong HREE-carbonate complexes are present in solution (Smrzka et al., 2019) but unlikely in the Archean oceans with low concentrations of CO_3^{2-} (where Archean oceans had a pH of ~ 6.3–7.7; Krissansen-Totton et al., 2018). Therefore, high partition coefficients for REE coprecipitation and adsorption (i.e., log $k_d > 1$) onto carbonate minerals (specifically calcite) suggests negligible

REE fractionation (Zhong and Mucci, 1995), resulting in proportional uptake of elements relative to seawater (Bau, 1993).

Post-depositional processes, such as diagenesis and subsequent low-grade metamorphism, can convert primary mineral phases into the common BIF minerals seen today, (e.g., converting Fe-(oxy)hydroxides to magnetite and hematite, and amorphous silica/chert to quartz; Aftabi et al., 2021; Klein, 2005; Maynard, 2012; Spry et al., 2000). Carbonate minerals, on the other hand, do not change significantly during diagenesis and/or low-grade metamorphism (Aftabi et al., 2021; Maynard, 2012; Spry et al., 2000). Therefore, diagenesis and low-grade metamorphism have negligible influence on trace element patterns in closed systems and under low water/rock ratios (Bau, 1993). However, other post-depositional processes (i.e., weathering, and hydrothermal alteration), which can be responsible for converting magnetite to hematite and/or goethite and dissolution of other mineral phases, may have a significant impact of trace element signatures (Bau, 1993; Li et al., 2023). Therefore, this study investigates how hypogene and supergene alteration affects the suitability of whole-rock and mineral fraction analyses for paleo-environmental reconstructions.

3. Geological setting

Archean BIF samples used in this study come from the Weld Range greenstone belt, located about 60 km NNW of the Cue townsite, in the Murchison Domain of the Youanmi Terrane, Yilgarn Craton, Western Australia. The greenstone belt has been metamorphosed to lower-greenschist facies (300 ± 50 °C, < 2–3 kbar; Gole, 1980) and comprises felsic crystal tuff, tuffaceous siltstones, felsic volcanic and volcaniclastic rocks, BIF, and mafic–ultramafic intrusions. Granitic rocks intrude the greenstone belt to the north and south (Fig. 1; Duuring and Hagemann, 2013a; Duuring and Hagemann, 2013b; Duuring et al., 2018; Van Kranendonk and Ivanic, 2009; Van Kranendonk et al., 2013; Wingate et al., 2013). The Beebyn BIF-hosted iron deposit is located along the southern margin of the greenstone belt, coinciding with Fe-enriched BIF of the Wilgie Mia Formation, with steeply dipping BIF macrobands extending along a NW-SE strike for up to 70 km (Fig. 1). The Madoonga deposit located along the northern margin of the greenstone belt is hosted by BIF of the Madoonga Formation.

The oldest dated rocks in the greenstone belt are 2977 ± 3 Ma felsic crystal tuff of the Madoonga Formation (Wingate et al., 2013). These rocks are unconformably overlain to the SE by rocks, including the Weld Range BIF, of the Wilgie Mia Formation from the Polelle Group. The Wilgie Mia Formation conformably overlies the ca. 2761–2735 Ma Greensleeves Formation, is intruded by the mafic–ultramafic ca. 2792–2741 Ma Gnanagooragoo Igneous Complex, and is unconformably overlain by ca. 2730 Ma felsic volcanic and volcaniclastic rocks, and siliciclastic rocks of the Glen Group farther south (Duuring et al., 2020; Van Kranendonk and Ivanic, 2009; Van Kranendonk et al., 2013; Wingate et al., 2013). As a result of the difficulty in determining precise ages of BIF (Goldich, 1973), based on age relationships between surrounding lithologies the Weld Range BIF is proposed to be ca. 2.73 Ga. The Weld Range BIF are representative of Algoma-type BIF based on their Archean age and affiliation with greenstone belts (Gross, 1990; Gross, 1980; Gross, 1983; Hagemann et al., 2016); they are interpreted to have formed within periodically quiescent basins with *syn*-depositional volcanism (Czaja et al., 2018). After primary deposition, BIF in the Weld Range greenstone belt was metamorphosed to lower-greenschist conditions, and experienced multiple deformation and alteration events, resulting in regional folding of BIF macrobands, and local secondary Fe enrichment.

Seven distinct stages of hypogene alteration, followed by near-surface supergene weathering, are locally recorded by BIF in the

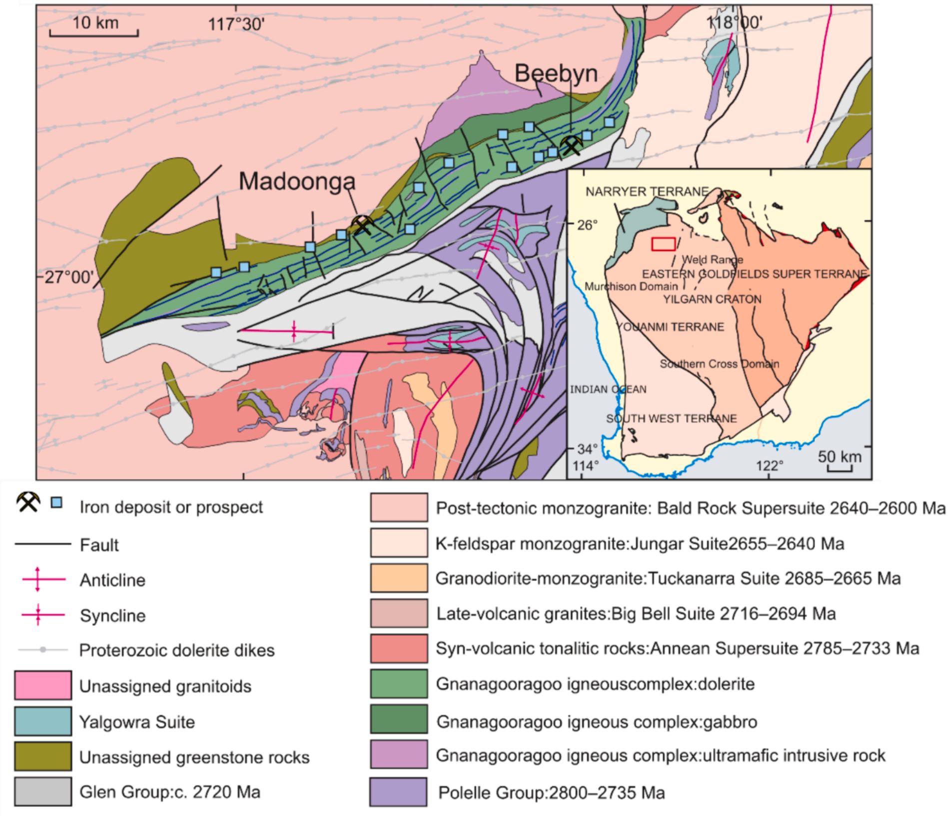

Fig. 1. Geological map showing the distribution of BIF, and surrounding lithologies, within Weld Range located in the northern Yilgarn Craton, Western Australia. Blue lines within the Gnanagooragoo igneous complex indicate banded iron formations. Modified from Duuring et al. (2018).

Beebyn and Madoonga deposits (detailed explanations and descriptions are found in: Duuring and Hagemann, 2013a; Duuring and Hagemann, 2013b; Duuring et al., 2018). At Beebyn, Stage 1 hypogene alteration resulted from the interaction between BIF and magmatic-derived fluids and minimal Archean seawater at high temperatures (i.e., > 440 °C) and elevated CO_2 (demonstrated by the precipitation of carbonate minerals; Duuring et al., 2018). Stage 2 hypogene alteration fluids recorded varying temperature and salinity conditions over time as the magmatic fluid was progressively diluted by Archean seawater (Duuring et al., 2018). During this stage, primary silica bands were comprehensively replaced by hypogene carbonates. Stage 3 hypogene alteration was facilitated by a > 98–175 °C fluid with low- to high-salinities, which is characteristic of vent fluids and heated Archean seawater that was chemically-modified (Duuring et al., 2018). This stage was mostly responsible for the removal of carbonate minerals and the enrichment of residual Fe-rich bands to form high-grade iron ore. Subsequent hypogene alteration events (i.e., Stages 4–7) were dominated by seawater and meteoric fluids, with fluid chemistry strongly influenced by the Archean ocean (Duuring et al., 2018). These stages were not responsible for further Fe enrichment but modified the oxidation state of the Fe oxides converting magnetite to hematite.

The Beebyn and Madoonga deposits record different mineral paragenesis sequences (Table 1). At Beebyn, early hypogene alteration resulted in the replacement of primary silica-rich bands by siderite during Stage 1 and ferroan dolomite (ankerite) during Stage 2. Stage 3 resulted in the leaching of the Stage 1 and 2 carbonate minerals with local precipitation of hypogene magnetite and dolomite. Stage 4 alteration was characterised by the replacement of Stage 2 and 3 dolomite by ferroan chlorite and the psuedomorphism of pre-existing magnetite by kenomagnetite. Similarly, Stage 5 alteration resulted in the replacement of Stage 2 and 3 dolomite by quartz and magnetite. Stage 6 and 7 alteration events at Beebyn precipitated ferroan dolomite-calcite and siderite-chlorite-magnetite assemblages (Duuring and Hagemann, 2013b).

Stage 1 hypogene alteration at the Madoonga deposit saw the precipitation of kenomagnetite (a pseudomorph of magnetite) and subsequent replacement by hematite (Duuring and Hagemann, 2013a). Stage 2 was characterised by replacement of silica-rich bands by talc and hypogene magnetite (Duuring and Hagemann, 2013a). During Stage 3 alteration, early magnetite and Stage 2 magnetite were replaced by kenomagnetite and hematite. Silica-rich bands were replaced Stage 4 siderite, which, alongside Stage 2 magnetite-talc, was cut by Stage 5 ferroan chlorite (and minor pyrite). Stage 6 alteration at the Madoonga deposit was characterised by local replacement of silica-rich bands by Stage 6 quartz (Duuring and Hagemann, 2013a).

Supergene alteration in BIF is observed mostly within 100 m of the present-day ground surface. Primary and hypogene mineral assemblages (i.e., carbonate, Fe oxide and silicate minerals) are locally replaced by goethite and hematite (Duuring and Hagemann, 2013a; Duuring and Hagemann, 2013b).

4. Methods

4.1. Sampling strategy

Hand specimens of BIF from the Weld Range greenstone belt were

Table 1
Alteration assemblages in hypogene-, and supergene-altered Weld Range BIF.

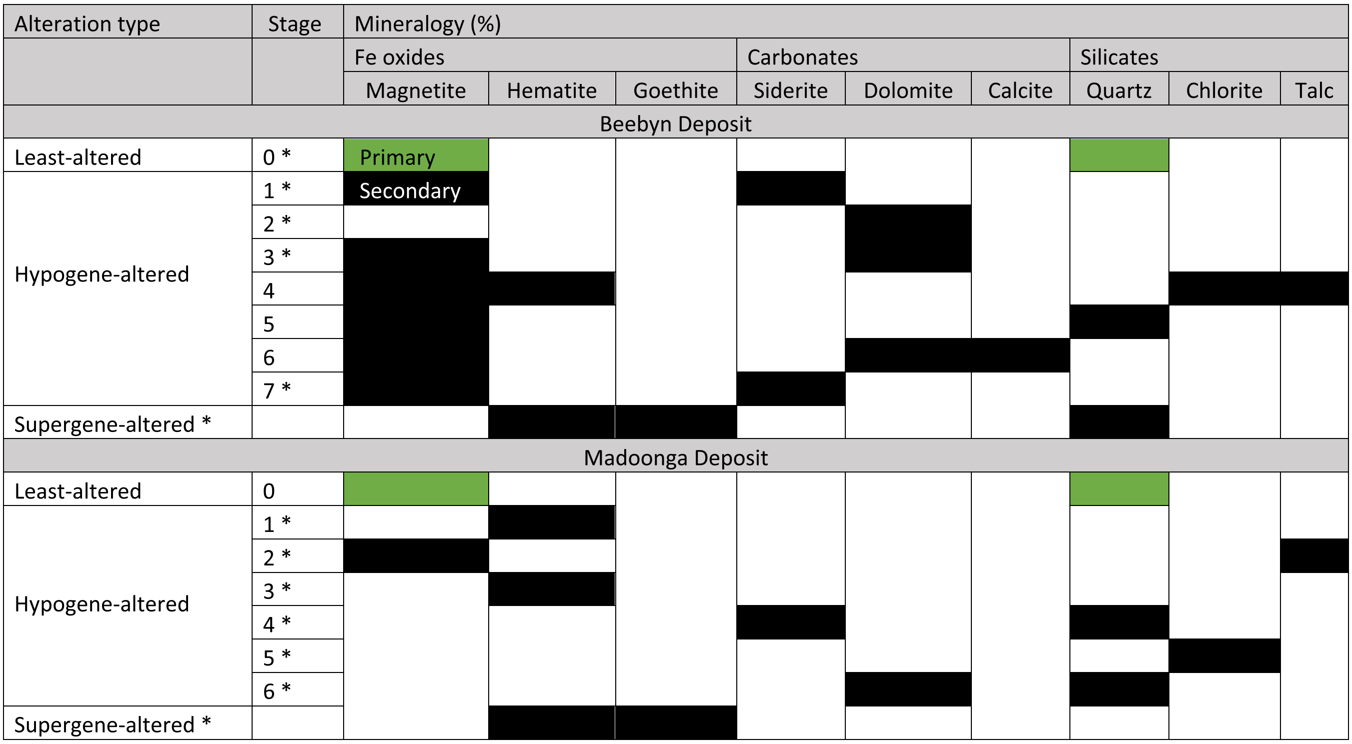

Alteration type	Stage	Mineralogy (%)								
		Fe oxides			Carbonates			Silicates		
		Magnetite	Hematite	Goethite	Siderite	Dolomite	Calcite	Quartz	Chlorite	Talc
Beebyn Deposit										
Least-altered	0 *	🟩 Primary						🟩		
Hypogene-altered	1 *	■ Secondary			■					
	2 *					■				
	3 *	■				■				
	4	■	■						■	■
	5	■						■		
	6	■				■	■			
	7 *	■			■					
Supergene-altered *			■	■				■		
Madoonga Deposit										
Least-altered	0	🟩						🟩		
Hypogene-altered	1 *		■							
	2 *	■								■
	3 *		■							
	4 *				■			■		
	5 *								■	
	6 *					■		■		
Supergene-altered *			■	■						

Alteration styles at the Beebyn and Madoonga deposits differ, assemblages shown are simplified from Duuring and Hagemann (2013b), Duuring and Hagemann (2013a) and Duuring et al. (2018). Primary and secondary minerals across these studies were differentiated through petrographic analyses of inter-mineral relationships (i.e., interlocking of grains and preservation of banding) and mineral grain sizes, as well as geochemical analyses. Further information on identifying minerals from various alteration stages at Weld Range is provided in Duuring and Hagemann (2013b), Duuring and Hagemann (2013a) and Duuring et al. (2018). Further information on identifying primary and secondary minerals, and alteration stages, for the samples within this study is provided in the Supplementary Material. Note: * refers the alteration styles present in samples analysed herein.

]

provided by the Geological Survey of Western Australia. Samples were analysed from different drill holes and depths across the Beebyn and Madoonga deposits (Table 3). This sampling strategy allowed the comparison of how alteration styles, sample depths, and regional geochemical variations may affect paleo-environmental reconstructions in the Weld Range BIF. An assorted collection of BIF from Australia, India and South Africa were used in addition to the Weld Range BIF to optimise sequential extraction methodology and facilitate comparison with other examples of least-altered and altered BIF. Sample descriptions and coordinates are provided in the Supplementary Material (sections S2, S3 and S4).

4.2. *Whole-rock analytical techniques*

Sample preparation was undertaken at James Cook University (JCU). Samples were crushed using a Rocklabs hydraulic tungsten-carbide rock splitter, the crushed material was sieved to obtain fragments $\leq$ 5 mm and $\geq$ 0.5 mm, which were milled into fine rock powders, following a pre-contamination step, using a Retch PM 100 planetary ball mill fitted with an agate insert. Mineralogy of samples was determined through X-Ray diffraction (XRD) at the University of Tasmania (UTas), where crystalline mineral phases were identified through their unique X-Ray wavelengths. Samples were analysed over a range of 4–100 $^{\circ}$ 2 θ using a CoKa radiation source on a Bruker D2Phaser Bragg-Brentano diffractometer. The diffractometer is equipped with an Fe K-beta filter, divergence slit, incident- and diffracted-beam Soller slits of 2.5 $^{\circ}$ and a LynxEye detector. The Co X-Ray tube was operated at 30 kV and 10 mA. Whole-rock major oxides were measured through X-Ray fluorescence (XRF) at UTas, using a PANalytical Axios Advanced X-Ray Spectrometer with 4 k Max Rh anode end window and 3 k Max Au end window X-Ray tubes. Volatile element contents (i.e., C, H and S) were measured on approximately 10 mg aliquots using a Thermo FlashSmart Elemental Analyser at UTas.

The remaining analytical work was conducted at the IsoTropics Geochemistry Laboratory, JCU. Whole-rock trace element analyses were conducted following a conventional HF-HNO_3-HCl digestion. Samples of ~ 50 mg were weighed into PFA vials and digested using 0.5 mL 29 M HF and 1 mL 16 M HNO_3 at 120 °C for 48–72 hrs. The samples were then dried and redissolved with 2 mL 6 M HCl at 120 °C for 24 hrs, then dried down again and brought into solution with 4 mL 2 M HNO_3. Samples were diluted by a factor of 20 using 2 % HNO_3 before being analysed using a Thermo Fisher iCAP^{TM} triple quadrupole inductively coupled plasma mass spectrometry (TQ-ICP-MS).

For trace element analyses, 6-point calibration was undertaken using gravimetrically measured calibration standards (i.e., zero-point blank, 0.5 ppb, 1 ppb, 5 ppb, 10 ppb, and 20 ppb). Each analysis was preceded by one minute of washout. Instrument mass bias drift was corrected by both an internal Ru calibrant (10 ppb) and through 1-in-10 analysis of the well-characterised USGS basaltic refence material BCR-2. Replicate digestions and instrumental analyses of reference materials (IF-G, Fer-1, Fer-2, Fer-3, Fer-4) were undertaken to quantify the accuracy and precision of the trace elements measured herein (refer to Supplementary Material section S7 and Table S12). Focusing on the most widely characterised BIF standard IF-G, most elements are accurate to within ± 10 % previous determinations, with the REE (including Y) all within $\leq \pm$ 6 % to previous isotope dilution analyses (i.e., Baker et al., 2002).

4.3. *Fraction-specific analytical techniques*

Mineral fractions (i.e., carbonates, Fe oxides, and silicates) were separated and analysed through sequential extractions (Table 2). The methodology herein was optimised from that presented in Oonk (2017), which is a modification of the more general protocol developed in Poulton and Canfield (2005). The diverse Fe oxide mineralogy of the hypogene- and/or supergene-altered Weld Range BIF includes abundant magnetite, hematite, goethite, and minor pseudomorphs such as kenomagnetite, compared to pristine BIF, such as the Asbestos Hill BIF, which are dominated by only magnetite (Oonk et al., 2017). This has implications for Fe oxide digestions due to differences in Fe oxidation state. The oxalate digestion step that targets Fe oxide minerals requires the presence of Fe^{2+} to catalyse the reaction (Oonk et al., 2017; Panias et al., 1996; Suter et al., 1988; Taxiarchou et al., 1997). Therefore, the hematite- and/or goethite-rich samples in this study (i.e., hematite and goethite have an Fe oxidation state of Fe^{3+}) were digested under inert conditions to transform Fe^{3+} to Fe^{2+} and help catalyse Fe oxide digestion. Magnetite-rich samples were digested under both inert and oxic conditions to compare atmospheric effects on recoveries. An additional consideration herein, is the high proportion (>50 %) of carbonate in some of the hypogene altered Weld Range BIF. Previously, Oonk et al. (2017) suggested that for carbonate-rich samples a smaller sample weight (i.e., 30 mg rather than 50 mg) may be more ideal to ensure complete carbonate-bound Fe digestions. Given testing herein (see section 6.1), 50 mg sample weight achieved better total recoveries (i.e., closer to 100 %) relative to 30 and 40 mg, therefore a sample weight of 50 mg is used in our experiments.

Table 2
Summary of reagents and conditions for targeting carbonates, Fe oxides and silicates in BIF through sequential extractions.

Target Fraction	Reagent	Conditions
Carbonates	1 M sodium acetate + 1.566 M acetic acid (pH = 4.5)	48 hr extraction at 50 °C in an inert atmosphere
Fe oxides	0.2 M ammonium oxalate + 0.17 M oxalic acid (pH = 3.2)	24 hr extraction at room temperature in an oxic atmosphere for magnetite-rich samples 24 hr extraction at room temperature in an inert atmosphere for hematite- and/or goethite-rich samples
Silicates*	29 M HF + 16 M HNO_3 + 6M HCl	48-72 hr digestion at 120 °C

Note: *The silicate-fraction comprises Si-rich phases (e.g. quartz, chert or Fe-silicates). On a chemical basis quartz (SiO_2) is an oxide mineral, however, mineralogically it is a tectosilicate with a structure comprised of silica (SiO_4) tetrahedra which are the framework of all other silicate minerals (Deer et al., 1966). Herein we consider quartz as part of the silicate-fraction due to its similar dissolution behaviour to other Si-rich phases/silicate minerals.

For the sequential extractions, 50 mg of rock powder was weighed into acid-leached 15 mL centrifuge tubes and individual mineral fractions were digested in the following order: carbonates, Fe oxides, and silicates, as per the protocol in Table 2. The carbonate-fraction was targeted by placing samples in an anaerobic chamber (98 % N_2, 2 % H_2) to prevent possible oxidation and formation of ferrihydrite on the surfaces of Fe-carbonate minerals (Oonk et al., 2017). Once placed in the anaerobic chamber, 10 mL of 1 M sodium acetate/1.566 M acetic acid (pH=4.5) was added to the samples. The samples were then sealed and removed from the chamber and placed horizontally in Ratek OM11 Orbital Shaking Incubator at 150 rpm and 50 °C for 48 hrs. Samples were then placed in a centrifuge at 3900 rpm for 10 mins, and then returned to the anaerobic chamber where the supernatant was pipetted, and syringe filtered (0.45μ m) into another acid-leached 15 mL centrifuge tube. The solid residue was washed with 10 mL MilliQ H_2O, placed at room temperature for 1 hr and then centrifuged, the MilliQ H_2O rinse was then decanted.

Iron oxide digestion was undertaken under either oxic or inert conditions (i.e., using the anaerobic chamber) depending on the mineralogy of the sample (Table 2). Magnetite-rich samples were digested under oxic conditions, whilst hematite- and/or goethite-rich samples were digested under inert conditions using the anaerobic chamber due to differences in Fe oxidation states. Once placed in the appropriate

Table 3
Summary of mineral proportions for Weld Range BIF and assorted BIF samples within this study, alongside sample names, prospects/localities, drill hole numbers, depth, and alteration styles.

Sample Name	GSWA #	Prospect	Drill Hole	Depth (m)	Alteration Stage	Mineralogy (%)						
						Quartz	Magnetite	Hematite	Goethite	Siderite	Ankerite-Dolomite	Chlorite/ Chamosite
Beebyn Deposit												
WR517	223517	W8	WRRC0335D	95.4	Least-altered	36.9	55.4				7.7	
WR504	223504	W7	WRRC1101D	184	Stage 1	37.9	21.1			41.0		
WR506	223506	W7	WRRC1101D	202	Stage 1*	53						47
WR508	223508	W7	WRRC1101D	212	Stage 1	35	36			29		
WR571	223571	W9	WRRC1076D	152.7	Stage 1	51.9	39			9		
WR572	223572	W9	WRRC1076D	160.5	Stage 1	56	40.4			3.6		
WR574	223574	W11	WRRC0676	178	Stage 1		42.5			35	22.5	
WR595	223595	W10	WRRC0253D	122.9	Stage 3	0.2	13.5	2.9			83.3	
WR541	223541	W8	WRRC1211D	125	Stage 7		15.7			84.3		
WR560	233560	W9	WRRD0583	163	Stage 7		69.1	24.1		6.8		
WR556	223556	W9	WRRD0583	150	Supergene	17.9		62.2	19.9			
WR608	223608	W11	WRRD0488	55.5	Supergene			100				
Madoonga Deposit												
WR678	223678	W14	WRRC0969D	166.5	Stage 1 + 2	71.9	20.4	7.8				
WR681	223681	W14	WRRC0969D	183	Stage 1 + 2	71.3	16.9	11.8				
WR690	223690	W14	WRRC0969D	220	Stage 3 + 4 + 5 + 6	72	28					
Outcropping Samples												
WR825	223825			Outcrop 3	Supergene	22.4		42.1	35.6			
WR828	223828			Outcrop 1	Supergene				100			
WR830	223830			Outcrop 2	Supergene	37.4		62.6				
Sample	Locality				Alteration Style	Mineralogy (%)						
						Quartz	Magnetite	Hematite	Goethite	Siderite	Dolomite	Chlorite/ Chamosite
Assorted BIF Samples												
IF-WA	Unknown location, Western Australia				Pristine	46.8	43.4			8.7	1.1	
Bar-1	Barberton, South Africa				Supergene	29.3		12.8	57.9			
Yil-1	Yilgarn, Western Australia				Supergene	48.6		29.3	22.1			
Pil-1	Pilbara, Western Australia				Supergene	65.7		31.5	2.7			
Pil-2	Pilbara, Western Australia				Supergene	46.5		7.9	45.6			
Sin-1	Singhbhum, India				Supergene	52.2		44.3	3.5			
Sin-2	Singhbhum, India				Supergene	78.7		21.3				
Sin-3	Singhbhum, India				Supergene	40.3		57.9	1.8			

Note: *sample WR506 from the Beebyn deposit exhibits Stage 1 hypogene alteration alongside extensive chlorite/chamosite alteration facilitated by nearby faults (refer to Supplementary Material section S3).

environment, 10 mL of 0.2 M ammonium oxalate with 0.17 M oxalic acid (pH=3.2) was added to each sample. Samples were placed on the orbital shaker at room temperature for 24 hrs. Following the extraction, the supernatant was pipetted and filtered into another acid-leached tube, and the solid residue was then agitated and rinsed with MilliQ H_2O as described above. The residual silicate-fraction, after agitation and rinsing, was resuspended, and the tube washed, with 5 mL MilliQ H_2O and pipetted into a clean 7 mL PFA vial. The sample was dried down and then dissolved using a standard HF-HNO_3-HCl digestion, as described above for whole-rock samples.

Major and trace element concentrations of each mineralogical fraction were analysed using an Agilent 5900 ICP-optical emission spectroscopy (ICP-OES) and TQ-ICP-MS, respectively. Major and trace element concentrations of the carbonate and Fe oxide fractions were measured using dilution factors of 50 and 10 with 2 % HNO_3, respectively. Matrix differences (e.g., correcting for the use of acetate and oxalate reagents) were accounted for by developing reagent-unique calibration standards and the BCR-2 reference material. Otherwise, the analysis protocol was as described above for the whole-rock analyses.

Recoveries of sequential extractions were calculated by the summation of major oxides (measured by the ICP-OES) in each mineral fraction with a detailed procedure provided in the Supplementary Material (section S1 and Table S3-5). Whilst using oxic conditions for the Fe oxide digestion step total recoveries in hypogene and supergene altered samples were extremely variable ranging from 77 % up to an extremely unrealistic 219 % (n = 62). When inert conditions were utilised instead the total recoveries improved markedly ranging from 77-164 % (n = 15). However, incomplete digestions of a mineral fraction under inert conditions persisted and resulted in unrealistically high total recoveries (i.e., > 120 %). Therefore, we have only considered experiments with total recoveries of 100 ± 20 % as valid and suitable for further interpretations (n = 20). In sequential extraction experiments it is common for total recoveries to exceed 100 % (i.e., Ho and Evans, 2000; Li et al., 2010; Oyeyiola et al., 2011; Vieira et al., 2009). For example, by comparing three different sequential extraction protocols for costal sediments, Oyeyiola et al. (2011) found that most overall recoveries were between 85–115 %, but some ranged up to 130 %.

Mineral fractions that consist of < 5 % of the whole-rock have also been omitted from data interpretation, given that relatively small fractions (i.e., < 5 %) result in higher uncertainties due to more elements approaching the detection limit and the greater proportional effects of aliquoting errors. For the Weld Range BIF, this was mostly for the carbonate-fraction in altered samples (e.g., hypogene-altered WR678 and WR681). The majority of total REE recoveries relative to the whole-rock ranged from ∼ 75–110 %, with better recoveries seen with increasing atomic mass (i.e., better recoveries and smaller range for HREE relative to LREE; Fig. 8c). Similar trends were seen by Lin et al. (2018), who attributed this to the better extraction efficiencies for the HREE in the oxalate reagent coupled with the HREE enrichment of the Fe oxides. Further discussion on the optimisation of sequential extractions and its influence on recoveries is provided in Section 6.1.

5. Results

5.1. Mineralogy

Detailed sample localities and petrographic descriptions for the Weld Range and assorted global BIF samples are provided in the Supplementary Material (section S3 and S4). Sample names, drill hole information, depth, alteration style (in accordance with Table 1) and mineral proportions (derived from XRD) are provided in Table 3.

The Weld Range BIF exhibits a wide range of mineralogy from which three major groups are recognised, namely least-, hypogene- and supergene-altered BIF. Quartz is the major and only silicate mineral (n = 13/14; Table 3) in most of the Weld Range samples. Based on mineralogy, quartz comprise of 41 % of the least-altered BIF, and ranges from 0-72 % in the hypogene-altered samples, and 0–37 % in the supergene-altered samples (Table 3). Chlorite (chamosite), another silicate mineral, is only present in one sample WR506 with a proportion of 47 % and reflects intense alteration that occurred along a fault (see Supplementary Material section S3). Therefore, due to extensive chlorite alteration, sample WR506 was omitted from paleo-environmental reconstructions. Common Fe oxide minerals include magnetite, hematite, and goethite. Magnetite and/or hematite dominate in least- and hypogene-altered BIF, whereas hematite and/or goethite dominate in supergene-altered BIF. For example, in hypogene-altered BIF (excluding WR506) magnetite proportions range from 14-69 % with hematite subordinate ranging from 3-24 %. Conversely, in supergene-altered BIF where magnetite is absent, hematite (up to 100 %) and/or goethite (up to 100 %) dominate, often comprising a significant proportion of the sample (Table 3). In hypogene-altered BIF relative proportions of carbonate, Fe oxide and silicates are highly variable (Fig. 3). Carbonate minerals (i.e., siderite and dolomite) are present in some hypogene-altered samples, such as samples WR504 and WR595, with mineral proportions of siderite and dolomite/ankerite ranging up to 84 % (Table 3). The least-altered BIF (WR517) also contains minor dolomite/ankerite at ∼ 8 %. In supergene-altered samples, where Fe oxides dominate, silicate mineral proportions rapidly decrease as Fe oxide contents increase, and carbonate minerals are absent.

The assorted collection of global BIF from Australia, India, and South Africa (n = 8) provide comparative examples of both pristine (i.e., IF-WA) and supergene-altered samples (i.e., Bar-1, Yil-1, Pil-1, Pil-2, Sin-1, Sin-2, and Sin-3). The pristine sample IF-WA comprises significant amounts of silicate, Fe oxide and carbonate minerals (quartz = 47 %, magnetite = 43 %, siderite = 9 %, and dolomite = 1 %), whereas the supergene-altered samples are dominated by quartz (30–79 %), hematite (8–58 %) and goethite (2–58 %), without carbonate minerals.

5.2. Whole-rock major elements

Significant whole-rock major element variability is observed within the Weld Range suite (Fig. 2 and Fig. 3). For example, the least-altered BIF (WR517) has a Fe_2O_3 content of 55 wt%, while Fe_2O_3 contents of hypogene altered samples varied from 30 to 87 wt% (median = 78 wt%), whereas the supergene-altered samples generally had higher Fe_2O_3 contents, ranging from 57-95 wt%. Higher Fe_2O_3 contents in supergene-altered samples are due to replacement of carbonate and silicate minerals largely by Fe oxides (i.e., hematite and goethite; Table 1 and Table 3; Duuring and Hagemann, 2013a; Duuring and Hagemann, 2013b; Duuring et al., 2018). Variable Fe_2O_3 contents in hypogene-altered samples reflect variable dissolution and precipitation of minerals corresponding to different alteration styles across the Beebyn and Madoonga deposits (Table 1). Silica contents range from 0-66 wt% and are inversely correlated with Fe_2O_3 content (Fig. 2b). Therefore, SiO_2 content is generally lower in supergene-altered samples, ranging from 0-40 wt%. However, some hypogene-altered samples that experienced

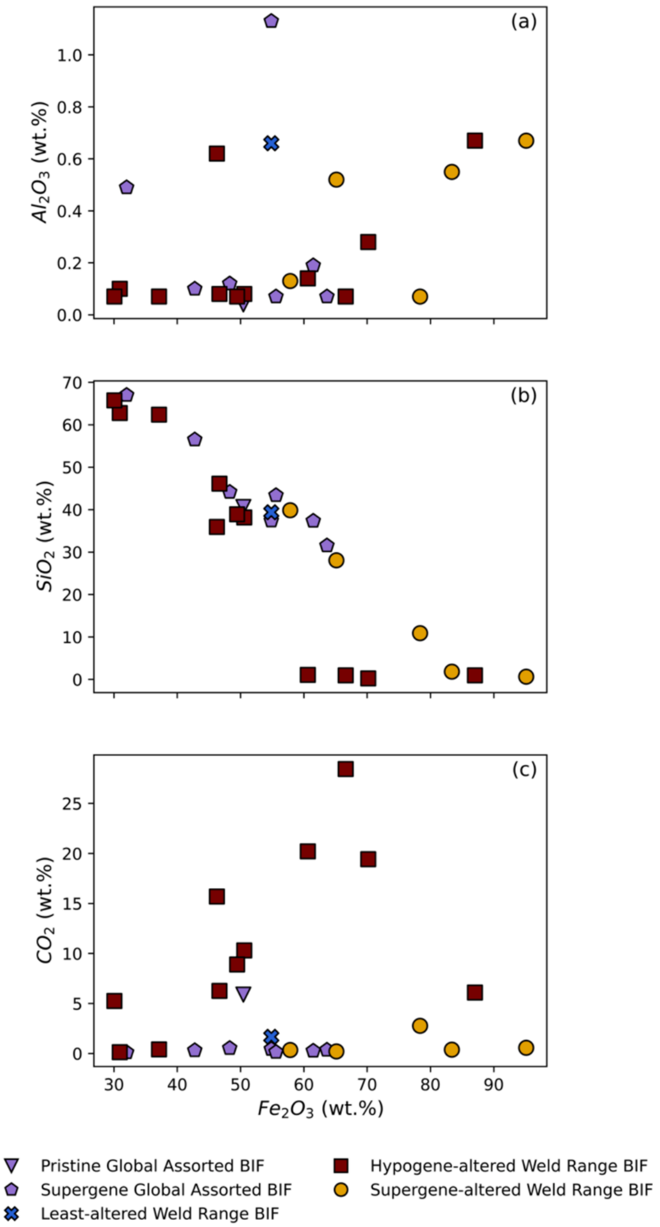

Fig. 2. Major oxide distribution of least- (blue), hypogene- (maroon), and supergene-altered (gold) Weld Range samples and the collection of assorted BIF samples from Australia, India and South Africa (for method validation; purple). Poor correlation between Al_2O_3 and Fe_2O_3 (a) argues against clastic controls for the least-altered and altered Weld Range BIF. Strong correlation between SiO_2 and Fe_2O_3 (b), alongside higher Fe_2O_3 proportions in altered Weld Range BIF, suggest that progressive hypogene and supergene alteration facilitates dissolution of silicates and secondary precipitation of Fe oxides. Similarly, the CO_2 (c) content across Weld Range samples is somewhat controlled by Fe_2O_3 content, where progressive alteration stages favour the dissolution of carbonates and secondary precipitation of Fe oxides.

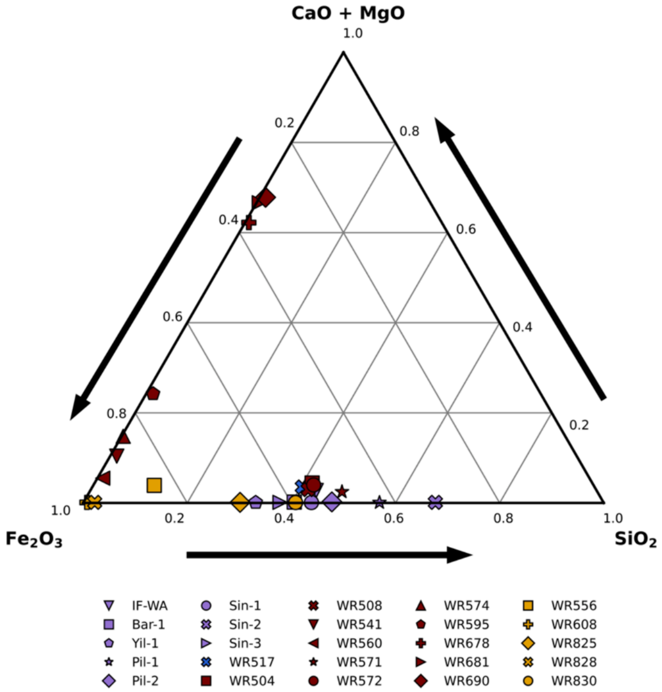

Fig. 3. Ternary diagram of CaO + MgO, Fe_2O_3 and SiO_2 of least- (blue), hypogene- (maroon), and supergene-altered (gold) Weld Range samples and the collection of assorted BIF from Australia, India and South Africa (purple). The distribution of samples is in the ternary diagram are strongly controlled by alteration styles, where progressive hypogene and supergene alteration favour the dissolution of silicates and carbonates (low SiO_2 and CaO + MgO contents, respectively) and the secondary precipitation of Fe oxides (high Fe_2O_3).

complete dissolution/replacement of quartz also demonstrate very low SiO_2 contents (e.g., samples WR541, WR560, WR574, and WR595 have SiO_2 contents < 1 wt%; Table 4). Carbon dioxide contents do not demonstrate a clear relationship with Fe_2O_3 (Fig. 2c), although elevated CO_2 contents are synonymous with increased MnO, MgO, and CaO concentrations (Supplementary Material Table S1) as they reflect an increased abundance of carbonate minerals. Least-altered Weld Range BIF exhibits a CO_2 content of 1.67 wt%. High CO_2 contents are restricted to hypogene-altered BIF, such as WR541 with a CO_2 content of 28 wt% (Table 1; Table 3; Fig. 2c, Supplementary Material Table S1). Conversely, supergene-altered BIF have low CO_2 contents (CO_2 content ranging from 0-3 wt%) due to dissolution of carbonate minerals during supergene weathering.

Most Weld Range BIF have low Al_2O_3 (<1 wt%), with no clear relationship observed between Al_2O_3 content and Fe_2O_3 content and therefore no clear relationship between Al_2O_3 and alteration type (Fig. 2a). Sample WR506 is anomalous with extremely elevated Al_2O_3 (15.6 wt%), TiO_2 (0.68 wt%), Na_2O (0.16 wt%) and K_2O contents (1.09 wt%) due to extreme chlorite/chamosite alteration and was omitted from further consideration. The pristine and supergene global BIF samples used for comparison possess similar major oxide compositions to comparable Weld Range BIF (Fig. 2).

5.3. Whole-rock trace elements

Whole-rock trace element signatures demonstrate that least-, hypogene-, and supergene-altered samples all potentially reflect seawater chemistry (Table 4; Fig. 4). The samples demonstrate seawater characteristics, such as shale-normalised LREE depletions relative to HREE (i.e., $Nd/Yb_{SN}<1$; $_{SN}$ subscripts refer to PAAS-normalised values), positive La_{SN} anomalies (i.e., $Ce/Ce^*_{SN}<1$) and Gd_{SN} anomalies (i.e., Gd/Gd*SN>1; Bau and Dulski, 1996; Ernst and Bau, 2021; Sylvestre et al., 2017; Thurston et al., 2012; Viehmann et al., 2015a). For example, least-altered BIF (WR517) has Nd/Yb_{SN}, Ce/Ce^*_{SN} and Gd/Gd^*_{SN} values of 0.48, 0.90 and 1.07, respectively. Hypogene-altered BIF values range from 0.30 to 0.63, 0.77–0.93 and 1.03–1.28, whilst supergene-altered BIF values range from 0.32 to 0.54, 0.62–1.14 and 0.95–1.23, respectively (Table 4).

Positive Y_{SN} ($Y/Y^*_{SN}>1$) and Eu_{SN} ($Eu/Eu^*_{SN}>1$) anomalies, and near to super-chondritic Y/Ho ratios (i.e., 27–90) are also indicative of seawater signatures in pristine BIF (Bau and Dulski, 1996; Ernst and Bau,

Table 4
Major oxide and trace element data for whole-rock Weld Range BIF and global assorted BIF

Sample	SiO_2	Al_2O_3	Fe_2O_3	Nd	Th/Sc	Ni/Lu	Nd/Yb_{SN}	Eu/Sm	Sm/Yb	Y/Ho	Ce/Ce^*_{SN}	Gd/Gd^*_{SN}	Eu/Eu^*_{SN}	Pr/Pr^*_{SN}	Y/Y^*_{SN}
WR504	35.92	0.62	46.27	3.96	0.174	286.891	0.416	0.483	1.301	28.80	0.898	1.025	2.518	0.781	1.156
WR506	50.59	15.55	22.71	15.86	0.399	496.4	0.687	0.260	1.586	26.76	0.998	0.915	1.456	0.975	1.064
WR508	38.15	0.08	50.59	2.14	0.080	271.878	0.463	0.550	1.422	31.29	0.846	1.162	2.686	0.790	1.247
WR517	39.39	0.66	54.85	2.974	0.203	126.302	0.481	0.501	1.458	28.79	0.904	1.070	2.532	0.816	1.142
WR541	0.95	0.07	66.62	2.716	0.021	1908.5	0.481	0.495	1.541	38.22	0.832	1.281	2.510	0.745	1.523
WR556	10.89	0.07	78.36	2.298	0.070	1270.8	0.376	0.580	1.330	33.69	0.787	1.225	2.758	0.684	1.329
WR560	0.94	0.67	87.03	2.581	0.047	374.3	0.385	0.552	1.232	38.14	0.830	1.148	2.583	0.740	1.535
WR571	46.11	0.08	46.67	3.104	0.099	291.745	0.629	0.556	1.904	32.06	0.925	1.164	2.942	0.825	1.232
WR572	38.89	0.07	49.46	1.785	0.108	361.364	0.341	0.622	1.110	37.38	0.835	1.146	2.954	0.752	1.524
WR574	0.24	0.28	70.18	4.943	0.294	137.685	0.462	0.526	1.316	33.43	0.907	1.049	2.664	0.825	1.353
WR595	1.06	0.14	60.64	4.85	0.043	42.14	0.412	0.584	1.446	32.36	0.850	1.114	2.876	0.715	1.273
WR608	0.65	0.67	95.12	4.535	0.078	253.160	0.459	0.393	1.391	29.77	0.721	0.996	2.014	0.863	1.176
WR678	62.36	0.07	37.13	0.929	0.045	134.082	0.303	0.808	0.761	50.80	0.769	1.055	3.296	0.838	2.221
WR681	62.76	0.1	30.94	0.938	0.032	56.525	0.318	0.788	0.945	40.91	0.795	1.243	3.153	0.760	1.685
WR690	65.73	0.07	30.09	1.696	0.016	111.891	0.479	0.526	1.221	39.37	0.798	1.216	2.394	0.825	1.612
WR825	28.06	0.52	65.13	3.733	0.171	123.782	0.540	0.459	1.772	24.82	1.142	1.130	2.533	0.691	0.957
WR828	1.82	0.55	83.38	13.503	0.032	399.077	0.441	0.403	1.727	24.32	0.615	1.187	2.132	0.662	0.929
WR830	39.85	0.13	57.84	1.182	1.150	37.646	0.319	0.515	0.924	32.62	0.943	0.945	2.493	0.791	1.342
IF-WA	40.63	0.04	50.44	1.701	0.148	62.461	0.579	0.521	1.107	59.12	0.684	1.203	2.195	0.903	2.584
Bar-1	37.39	1.13	54.85	4.603	0.211	436.886	0.302	0.550	0.955	37.25	0.868	1.077	2.370	0.745	1.539
Yil-1	31.53	0.07	63.65	1.33	0.194	116.652	0.370	0.502	0.806	51.18	0.775	1.017	2.234	0.875	2.262
Pil-1	56.49	0.1	42.77	8.947	0.110	67.111	2.498	0.323	4.925	45.86	0.836	1.405	1.536	0.941	1.569
Pil-2	44.15	0.12	48.29	2.736	0.220	151.835	0.241	0.685	0.800	38.75	1.133	1.063	3.001	0.635	1.649
Sin-1	43.38	0.07	55.59	0.458	0.175	237.326	0.348	0.295	3.076	30.20	1.168	1.979	1.409	0.266	1.038
Sin-2	66.99	0.49	32.01	3.192	3.835	193.477	1.598	0.254	6.735	26.87	0.518	2.248	1.217	0.506	0.875
Sin-3	37.34	0.19	61.48	2.506	1.104	104.858	1.282	0.232	2.586	36.32	0.649	1.173	1.267	1.044	1.338

Major oxides (SiO_2, Al_2O_3, and Fe_2O_3) are provided in wt.%. Trace elements (Nd) are provided in ppm. Shale-normalised ($_{SN}$) data was normalised using values from Pourmand et al. (2012). Equations used for calculating anomalies are provided in the Supplementary Material section S5.

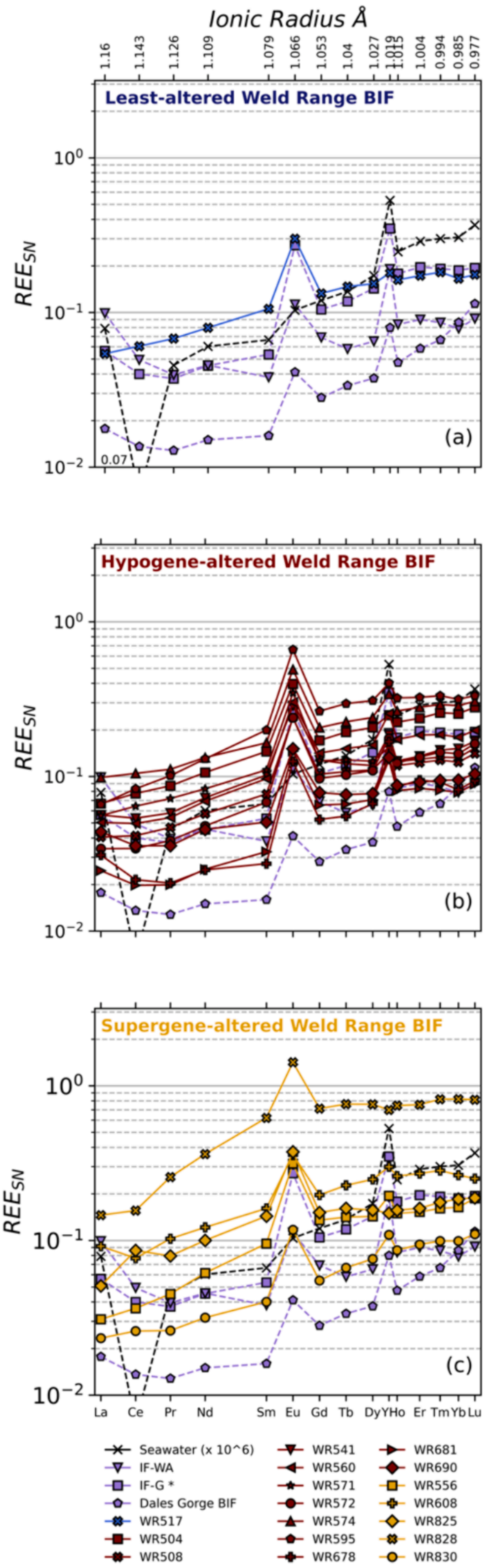

Fig. 4. Whole-rock REE distribution of least- (blue; a), hypogene- (maroon; b), and supergene-altered (gold; c) Weld Range samples, reference studies and standards; Dales Gorge BIF (Pecoits et al., 2009) and IF-G (* values used are provided in the Supplementary Material Table S9), seawater (Alibo and Nozaki, 1999), and IF-WA from the collection of assorted BIF (purple). Data is normalised to post Archean Australian shale (PAAS) using values from Pourmand et al. (2012). Overall, the least-, hypogene- and supergene-altered Weld Range BIF demonstrate positive Eu and Y anomalies, which are characteristic of hydrothermal input and seawater in BIF, respectively.

2021; Sylvestre et al., 2017; Viehmann et al., 2015a). Positive Y anomalies reflect rapid precipitation of BIF, where REE are removed too rapidly to allow for equilibrium between the precipitate and the seawater, therefore inhibiting REE fractionation. Near- to super-chondritic Y/Ho ratios, on the other hand, reflect the primary origin of banding in the BIF, rather than a post-depositional origin that would drive lower Y/Ho ratios (particularly in Fe oxide-dominant samples) due to Ho scavenging by Fe (oxy)hydroxides. Whereas positive Eu anomalies reflect the influence of high-temperature vent fluids. In the least-altered BIF WR517 Y/Ho = 28.8, while hypogene- and supergene-altered BIF generally range to higher values from 28.8 to 50.8 and 24.3–33.7, respectively (Fig. 6d; Fig. 10a,c). All Weld Range BIF samples demonstrate positive Eu_{SN} anomalies (Eu/Eu^*_{SN}=2.01–3.30; Fig. 6b) with most samples having a positive Y_{SN} anomaly, except for supergene altered BIF WR825 (0.96) and WR828 (0.93).

5.4. Fraction-specific trace elements

Fraction-specific data (i.e., carbonate-, Fe oxide-, and silicate-fractions) and total elemental recoveries are provided for a selection of samples in Table 5, with the complete dataset provided in the Supplementary Material (Table S6). According to alteration assemblages in Table 1, as well as XRD analyses performed within this study, siderite, dolomite, and calcite comprise the carbonate-fraction, and magnetite, hematite, and goethite comprise the Fe oxide-fraction. The silicate-fraction comprises quartz/chert/amorphous silica and contains negligible Fe-silicates, chloride or talc within the samples selected for this study (excluding WR506, which was omitted from further interpretation due to extensive chlorite alteration). Unfortunately, sequential extractions did not work properly for the supergene-altered Weld Range BIF due to incomplete digestion of the Fe oxide-fraction and therefore they will not be discussed further below.

5.4.1. Carbonate-fraction

The carbonate-fraction of the least-altered BIF (WR517) demonstrated seawater signatures, where Nd/Yb_{SN}, Ce/Ce^*_{SN}, and Gd/Gd^*_{SN} values were 0.26, 0.71, and 1.07, respectively. The least-altered BIF also exhibits a positive Eu_{SN} anomaly (Eu/Eu^*_{SN}=3.10), as well as a Y/Ho value of 27.2. However, this sample lacks a strongly positive Y_{SN} (Y/Y^*_{SN}=1.09) anomaly. The carbonate-fraction of WR517 should be interpreted with caution due to the fraction representing only about 5 % of the whole-rock. Several hypogene-altered carbonate fractions have been omitted from formal analysis due to fraction proportions representing < 5 % of the whole-rock (e.g., WR678, WR681, and WR690) or incomplete digestions (e.g., WR560, WR574, WR595). The remaining hypogene-altered samples that have higher carbonate proportions (>5 %) strongly reflect seawater characteristics, with Nd/Yb_{SN}<1, Ce/Ce^*_{SN}<1, and Gd/Gd^*_{SN}>1. For example, sample WR508, which has a carbonate proportion of 20 %, exhibits a Nd/Yb_{SN} value of 0.16, a Ce/Ce^*_{SN} value of 0.65, and a Gd/Gd^*_{SN} value of 1.23. All hypogene-altered samples, similar to WR508 (Fig. 5c), demonstrated positive Eu_{SN} anomalies and no to minimal positive Y_{SN} anomalies. Yttrium/Ho values across the carbonate-fraction for hypogene-altered samples ranged from 27.3 to 34.3, largely reflective of near- to super-chondritic values (Fig. 10b,d).

5.4.2. Fe oxide-fraction

In the least-altered Weld Range BIF (WR517) the Fe-oxide fraction consisted of 44 % of the sample and provided partial evidence for preservation of seawater signatures. WR517 showed Nd/Yb_{SN}, Ce/Ce^*_{SN} and Gd/Gd^*_{SN} values of 0.16, 0.75 and 1.01, respectively, coupled with a strong positive Eu_{SN} anomaly (Eu/Eu^*_{SN}=2.82), whereas it lacked a positive Y_{SN} anomaly (Y/Y^*_{SN}=0.99) and had a low Y/Ho value (25.7). The proportions of Fe oxides, relative to the whole-rock, across hypogene-altered samples ranged from 12-32 %. Hypogene-altered samples demonstrate positive Eu_{SN} anomalies, weak to no Y_{SN}

Table 5
Trace element (ppm) rare earth element data for fraction-specific Weld Range BIF and assorted BIF samples.

Sample		La	Ce	Pr	Nd	Sm	Eu	Gd	Tb	Dy	Y	Ho	Er	Tm	Yb	Lu	Nd/Yb$_{SN}$	Ce/Ce*$_{SN}$	Gd/Gd*$_{SN}$
508	*a*	1.806	3.656	0.475	2.141	0.530	0.291	0.625	0.096	0.587	3.877	0.124	0.378	0.058	0.373	0.062	0.463	0.846	1.162
	b	0.558	1.219	0.179	1.118	0.351	0.262	0.494	0.077	0.484	3.136	0.114	0.370	0.069	0.582	0.126	0.155	0.650	1.230
	c		0.422	0.077	0.393	0.170	0.134	0.328	0.065	0.411	2.228	0.079	0.232	0.041	0.300	0.048	0.106		1.075
	d	1.993	3.701	0.471	2.191	0.503	0.290	0.613	0.098	0.605	4.128	0.130	0.385	0.055	0.312	0.042	0.567	0.811	1.106
	e	1.990	4.533	0.654	3.404	0.981	0.638	1.295	0.228	1.442	8.630	0.305	0.894	0.138	0.923	0.142			
517	*a*	2.413	5.341	0.688	2.974	0.727	0.364	0.802	0.131	0.818	4.925	0.171	0.532	0.082	0.499	0.077	0.481	0.904	1.070
	b	4.504	11.573	1.790	9.951	3.081	2.054	4.027	0.722	4.597	26.670	0.979	2.859	0.448	3.063	0.482	0.262	0.713	1.067
	c	0.099	1.014	0.173	1.057	0.415	0.281	0.673	0.134	0.883	4.502	0.175	0.525	0.082	0.532	0.070	0.160	0.752	1.005
	d	3.155	6.613	0.822	3.494	0.697	0.329	0.678	0.104	0.662	4.794	0.154	0.497	0.077	0.489	0.074	0.576	0.911	1.001
	e	1.747	4.025	0.522	2.374	0.569	0.308	0.678	0.118	0.765	4.705	0.164	0.515	0.081	0.523	0.075			
IF-WA	*a*	4.409	4.362	0.401	1.701	0.262	0.137	0.417	0.052	0.347	5.211	0.088	0.277	0.039	0.237	0.040	0.579	0.850	1.114
	b	2.258	2.816	0.333	1.866	0.427	0.303	0.876	0.120	0.830	11.301	0.217	0.658	0.099	0.746	0.149	0.202	0.824	0.987
	c	0.541	1.121	0.155	0.859	0.234	0.149	0.528	0.072	0.461	5.720	0.107	0.312	0.041	0.222	0.036	0.312		0.799
	d	4.231	4.143	0.365	1.448	0.183	0.085	0.257	0.031	0.228	3.766	0.063	0.211	0.030	0.173	0.028	0.677	0.733	1.314
	e	3.129	3.289	0.313	1.363	0.226	0.125	0.399	0.052	0.357	5.121	0.091	0.287	0.040	0.242	0.042			

Note: *a*, *b*, *c*, *d*, *e* refers to whole-rock, carbonate-fraction, Fe oxide-fraction, silicate-fraction, and total recovery concentrations, respectively. Total elemental recoveries from sequential extraction were calculated by the sum of trace element data from the mineral fractions, relative to the proportions of the mineral fractions.

anomalies, and near- to super-chondritic Y/Ho values ranging from 27.02 to 44.06. All hypogene-altered samples exhibited HREE enrichment (Nd/Yb$_{SN}$<1), positive La$_{SN}$ anomalies (Ce/Ce*$_{SN}$<1), and positive Gd$_{SN}$ anomalies (Gd/Gd*$_{SN}$>1).

5.4.3. *Silicate-fraction*

The silicate-fraction of least-altered BIF WR517 (52 % of the whole-rock), unlike the Fe oxide-fraction, demonstrates a clear positive Y anomaly (Y/Y*$_{SN}$ value of 1.30) and a super-chondritic Y/Ho (31.2) that is reflective of that observed in seawater (Ernst and Bau, 2021; Sylvestre et al., 2017), it also possess Nd/Yb$_{SN}$<1 (0.58) and Ce/Ce*$_{SN}$<1 (0.91). Similarly, the silicate-fractions of the hypogene-altered BIF have super-chondritic Y/Ho ranging from 29.99. to 51.32, positive Y anomalies (Y/Y*$_{SN}$ ranging from 1.22 to 2.32), and positive Eu anomalies (Eu/Eu*$_{SN}$>1). Furthermore, like seawater, the silicate fraction in all hypogene-altered samples possesses HREE enrichment (Nd/Yb$_{SN}$=0.23–0.63), as well as positive La and Gd anomalies (Ce/Ce*$_{SN}$=0.69–0.81; Gd/Gd*$_{SN}$=1.03–1.20; Table 5).

6. Discussion

6.1. *Optimising sequential extractions for BIF with diverse mineralogy*

Fraction-specific analysis of BIF with diverse mineralogy was optimised and validated through experimentation with the Weld Range and global assorted BIF sample suites herein.

6.1.1. *Effect of sample weight on carbonate recovery*

Previous sequential extraction studies (Oonk et al., 2017) suggested that a smaller sample weight (i.e., 30 mg) for carbonate-rich samples could potentially ensure complete digestion of carbonate-bound Fe. Here we investigated the effect of sample weight (30, 40 and 50 mg) on the total extraction recoveries for carbonate-rich (>20 %) BIF samples (WR508, WR541, WR574, and WR595) from Weld Range. Contrary to the previous suggestion, this study found that a larger sample weight of 50 mg resulted in better total recoveries than either 30 or 40 mg (Fig. 8a; e.g., WR541 total recoveries were 114 %, 132 % and 97 %, for sample weights of 30 mg, 40 mg, and 50 mg samples, respectively). A further complication with using smaller sample weights (e.g., 30 and 40 mg) is that it often resulted in incomplete digestions in the first two steps of the sequential extraction process (i.e., carbonate- and oxide-fractions) that resulted in significantly overestimated proportion for the silicate-fraction, relative to that expected from the whole-rock SiO_2 content. For example, mineralogical (XRD) analysis of WR541 determined the sample to be absent of silicate minerals, as supported by minor SiO_2 (<1 wt%) content. However, sample weights of 30 and 40 mg resulted in unrealistic silicate-fraction proportions of 27 % and 20 %, respectively. Using a sample weight of 50 mg resulted in a silicate-fraction proportion of a more realistic 8 %, this is still an overestimate given that WR541 is almost barren of silicate minerals. This suggests potentially incomplete digestion of one of the proceeding phases (i.e., Fe oxides or carbonates), although very close to the ideal margin of uncertainty for this type of sequential extraction work (~ ± 5 %). We suggest that future studies investigate larger sample weights (e.g., 100 mg) to further optimise sequential extractions for carbonate-rich samples, where larger sample weights will ensure a more representative sampling of the bulk material and should assist in catalysing the digestions.

Failure of the sequential extraction procedure does not appear to be systematically controlled by the proportion of carbonate minerals, namely that WR541 exhibited the highest carbonate content (85 %) and resulted in adequate fraction digestions. Similarly, digestion problems do not appear to be controlled by magnetite content, given that WR572 had the highest content of magnetite (40 %) across the hypogene-altered samples and this resulted in accurate mineral-fraction proportions and recoveries. Therefore, alongside investigating larger sample weights, we also suggest investigating the effect of an inert Fe oxide (oxalate)

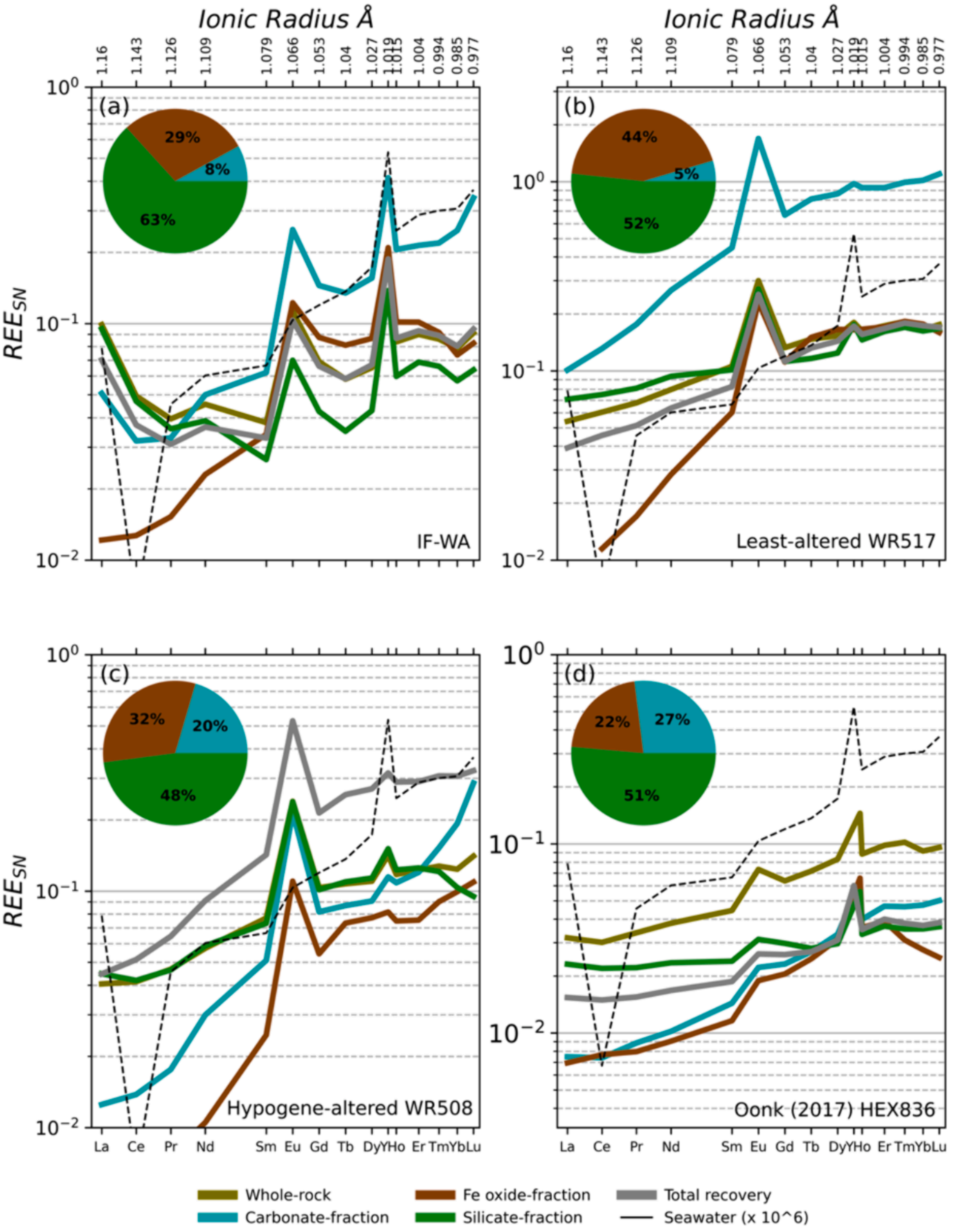

Fig. 5. Whole-rock, fraction-specific and total recovery REE distribution of IF-WA from the collection of assorted BIF (this study; a), WR517 and WR508 (this study; b and c) from Weld Range, and the distribution of sample HEX836 from the pristine Asbestos Hills BIF (d; Oonk et al., 2018; Oonk et al., 2017), normalised to Post Archean Australian Shale (PAAS) using values in Pourmand et al. (2012). Seawater values (x 10^6) from Alibo and Nozaki (1999) were used to compare REE patterns. Similar to whole-rock REE patterns, fraction-specific REE distributions also reflect positive Eu and Y anomalies that are typical of seawater signatures in BIF. Total recoveries of the Weld Range BIF and the collection of assorted BIF from Australia, Inida and South Africa were calculated by the sum of trace element data from the mineral fractions, relative to the proportion of the mineral fraction. Refer to the Supplementary Material (section S1) for further information on calculating total recoveries.

digestion for carbonate-rich samples. As Fe in magnetite is present as either Fe^{2+} or Fe^{3+}, in samples such as WR595 with minimal magnetite (24 %), this may be insufficient to properly catalyse the Fe oxide digestion. Therefore, it is suggested that the effect of inert versus oxic atmospheric conditions on carbonate-rich BIF samples should be investigated further.

6.1.2. *Effect of anoxic conditions on Fe oxide digestions and recoveries*

Previous sequential extraction schemes for Fe-rich sediments (i.e., Oonk et al., 2017; Poulton and Canfield, 2005), undertook amorphous and crystalline Fe oxide digestions with reagents, such as hydroxylamine-HCl, sodium dithonite, or ammonium oxalate. Oonk et al. (2017) demonstrated that using only ammonium oxalate under oxic conditions was effective in targeting the magnetite-rich Asbestos Hills BIF, with limited benefits of an additional sodium dithonite step due to limited hematite (and goethite) present in the samples. Herein, despite hematite and/or goethite dominated samples in some instances, it was prioritised to limit the number of extraction steps to minimise potential cross-contamination between fractions and analytical blanks. Therefore, Fe oxide digestions for both magnetite- and hematite-/goethite-rich samples through a singular oxalate digestion were attempted, with the efficiency of oxic and inert conditions compared.

In traditional oxalate digestions of magnetite under oxic conditions, Fe^{2+} present in the samples catalyses the digestions. However, BIF that are rich in hematite and goethite (minerals with an Fe oxidation state of Fe^{3+}) requires an inert atmosphere to reduce Fe^{3+} to Fe^{2+} and catalyse the reaction (Oonk et al., 2017; Panias et al., 1996; Suter et al., 1988; Taxiarchou et al., 1997). For example, in supergene-altered hematite-rich sample Bar-1 the Fe oxide-fraction was very poorly digested under oxic conditions for the Fe oxide step (as indicated by Fe oxide proportion of 10 %, despite the sample having 13 % hematite and 58 % goethite, and total recovery of 150 %), whereas using inert atmospheric conditions resulted in complete Fe oxide digestion (Fe oxide proportion of 48 % and total recovery of 92 %). For more pristine magnetite bearing IF-WA and Fer-4 samples, the inert conditions produced extremely comparable fraction recoveries (i.e., within ± 5 % of each other) to experiments conducted under oxic conditions (Fig. 9). Therefore, we suggest application of inert digestions for the Fe oxides step, which can be useful for more mineralogically complicated sample suites, as it is suitable for both magnetite and hematite/goethite rich samples.

6.2. *Assessing the effect of clastic contamination*

Excessive clastic contamination can affect the robustness of paleoenvironmental reconstructions from chemical sediments, due to the addition of exogenous elements from continental weathering fluxes. In BIF the influence of clastic contamination is generally identified by elevated concentrations and positive correlations between immobile elements, such as Al, Ti, Zr, Hf and REE (Alexander et al., 2009; Basta et al., 2011; Bau, 1993; Djoukouo Soh et al., 2021; Ernst and Bau, 2021; Oonk et al., 2017; Pecoits et al., 2009). However, in the literature there is not a universal ‘cut-off’ for clastic contamination applied, with different studies adopting different Al_2O_3 contents of 0.4 wt% (Ernst and Bau, 2021), 0.5 wt% (Delvigne et al., 2012; Wang et al., 2014) and up to

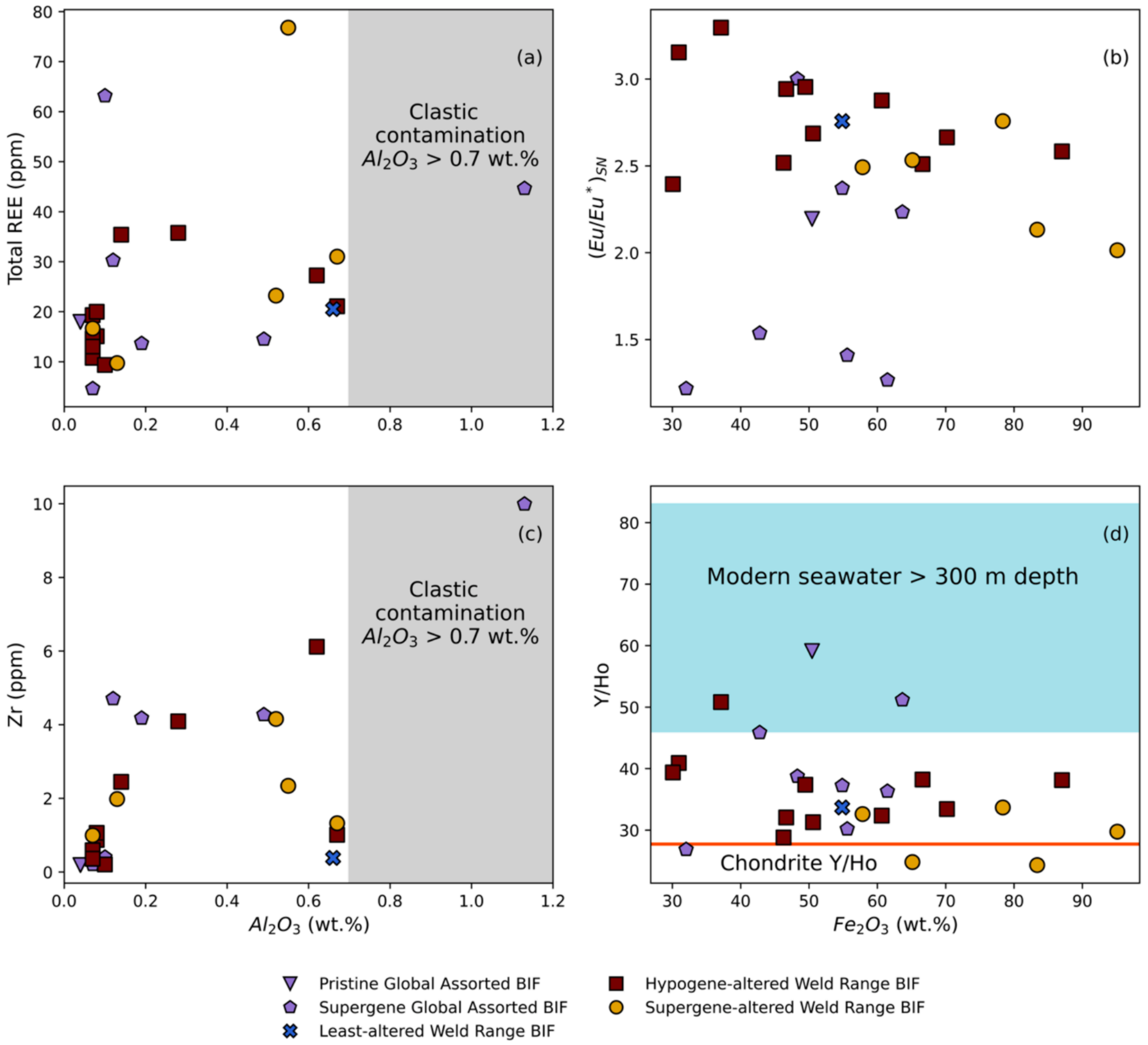

Fig. 6. Whole-rock major and trace element graphs indicating no distinct trends between both total REE (a; ppm) and Zr (c; ppm) with clastic contamination (Al_2O_3), suggesting that clastic contamination is negligible and does not influence REE signatures in the Weld Range BIF. Clastic contamination cut-off ($Al_2O_3 > 0.7$ wt.%) for this study, as explained in section 6.2, is indicated by the grey field. Lack of distinct trends between Eu/Eu^*_{SN} (b) and Y/Ho (d) relative to Fe_2O_3 across the Weld Range BIF suggests that with progressive hypogene and supergene alteration (and increased proportions of Fe_2O_3) seawater-like signatures are preserved. However, it is important to consider if these seawater-like signatures across hypogene- and supergene-altered BIF is primary. Yttrium/Ho ratio variability of modern seawater > 300 m depth provided by the light blue field (Y/Ho ratio ~45-85; Alibo and Nozaki, 1999; Ernst and Bau, 2021) and Y/Ho ratio of chondrite provided by the orange line (Y/Ho ratio of ~27.7; Sun and McDonough, 1989) in (d).

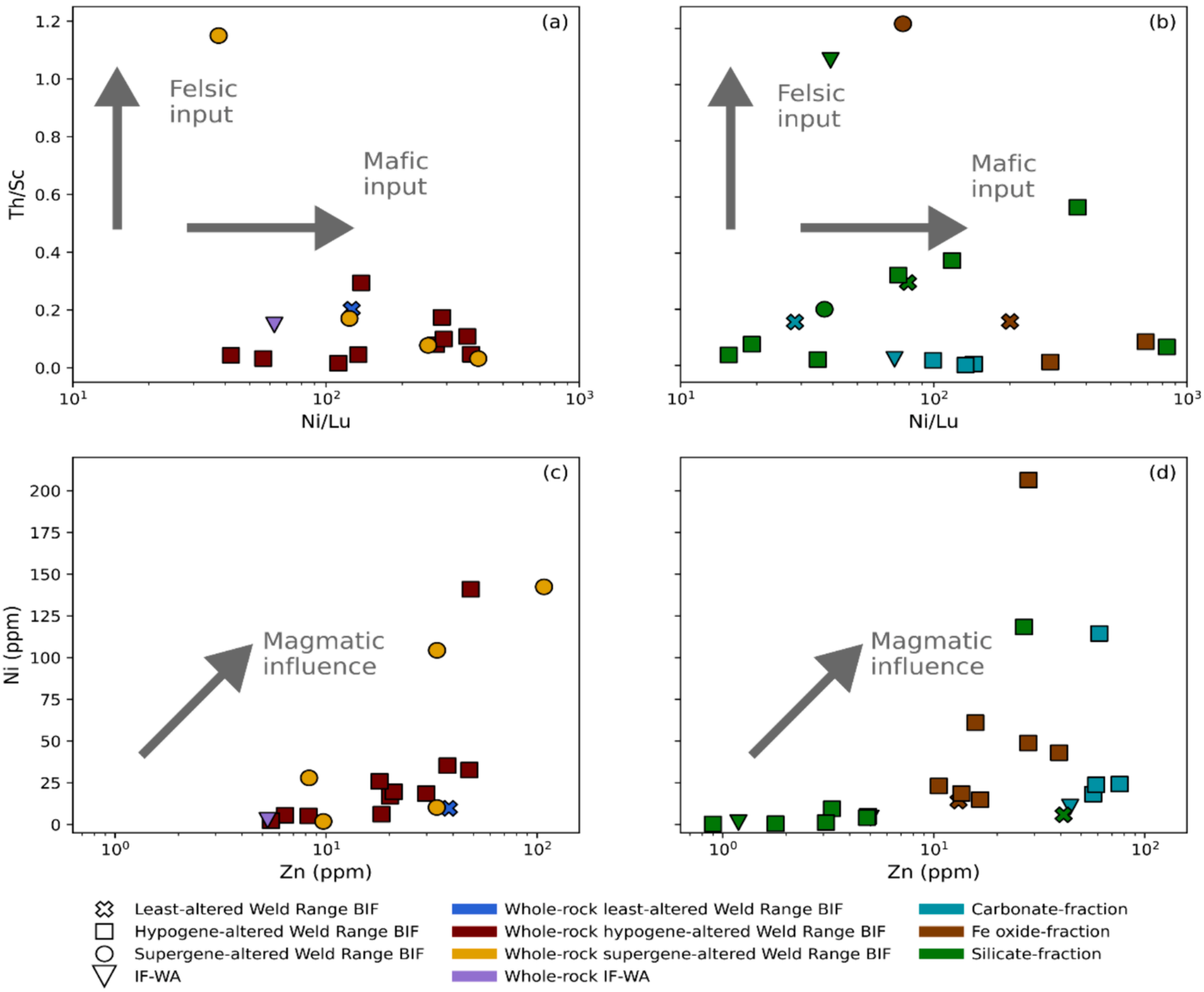

Fig. 7. Whole-rock and fraction-specific graphs indicating possible contamination by felsic and mafic input (Th/Sc vs Ni/Lu; a and b), where increasing Th/Sc reflects increasing felsic input and increasing Ni/Lu reflect increasing mafic input. The whole-rock and fraction-specific analyses of the Weld Range BIF suggest a greater mafic influence. The increasing influence of magmatic input across the whole-rock and fraction-specific Weld Range BIF was also observed through increasing Ni and Zn concentrations (c and d). Nickel and Zn were selected as magmatic influence tracers based on a systematic study of the alteration fluids at Weld Range (Duuring et al., 2018). Increasing magmatic input is observed across the carbonate- and Fe oxide-fractions in altered BIF, suggesting secondary magmatic Ni and Zn addition to these phases.

1 wt% (Konhauser et al., 2009; Lechte et al., 2019; Peng et al., 2018). Other studies (e.g., Baldwin et al., 2012; Haugaard et al., 2013; Viehmann et al., 2015b) acknowledge the implications of clastic contamination for paleo-environmental reconstructions but do not provide definitive ‘cut-off’ values, highlighting the lack of accepted ‘cut-off’ values for choosing samples suitable for paleo reconstruction purposes. This ambiguity is largely due to location-specific controls and intra suite variations in major and trace element signatures of different BIF. In this study, 65 % (n = 11/17) of the Weld Range samples have Al_2O_3 contents < 0.5 wt%, with the rest ranging up to ca. 0.7 wt% (Table 4). The Weld Range BIF samples display a weak positive correlation between Al_2O_3 and both Zr ($r^2 = 0.39$) and total REE ($r^2 = 0.22$) concentrations (Fig. 6), suggesting that the degree of clastic contamination in this sample suite, does not significantly control trace element signatures especially the REE. Consequently, the marginally elevated Al_2O_3 contents (up to 0.7 wt %) of a few samples has a minimal influence on undertaking paleo-environmental reconstructions using the Weld Range BIF.

6.3. Whole-rock paleo-environmental reconstructions and the effects of hypogene and supergene alteration in the Weld Range BIF

Whole-rock signatures from pristine BIF are commonly used to reconstruct ancient seawater chemistry due to their shale-normalised REE signatures being likened to shale-normalised REE modern seawater signatures (Alexander et al., 2009; Alexander et al., 2008; Bau, 1993; Bau and Dulski, 1996; Bolhar et al., 2004; Haugaard et al., 2016; Planavsky et al., 2010). However, very few studies have investigated the suitability of REE signatures of whole-rock compositions from altered BIF for paleo-environmental reconstructions (Li et al., 2023; Sampaio et al., 2018). Despite the Weld Range BIF undergoing extensive hypogene and supergene alteration (as described in Duuring and Hagemann, 2013a; Duuring and Hagemann, 2013b; Duuring et al., 2018), most samples still reflect seawater characteristics. These characteristics include, but are not limited to, positive La_{SN}, Eu_{SN}, $Gd_{SN,}$ and Y_{SN} anomalies, $HREE_{SN}$ enrichment relative to $LREE_{SN}$, and near- to super-chondritic Y/Ho values (i.e., Y/Ho values between 27–90; Bau and Dulski, 1996; Ernst and Bau, 2021; Sylvestre et al., 2017; Thurston et al.,

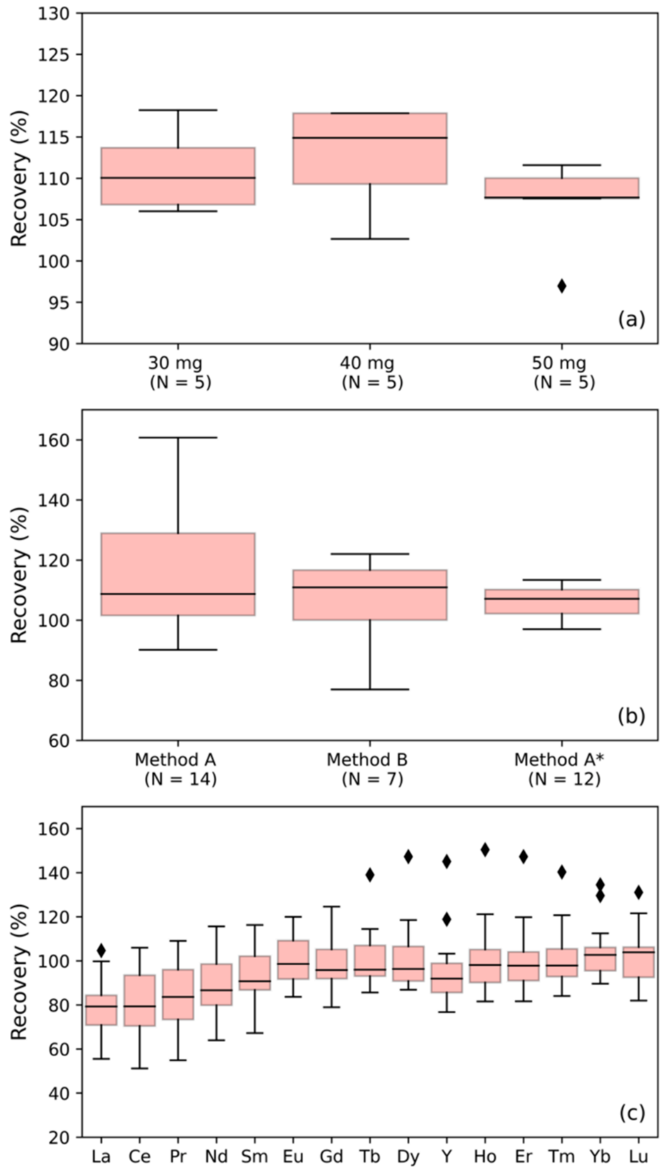

Fig. 8. Box and whisker plots of total (a and b) and elemental recoveries (c) of the sequential extraction experiments. (a) The effect of sample weight, where 50 mg is suggested to provide better (i.e., closer to 100%) and more reproducible recoveries than 30 and 40 mg. Samples WR574 and WR595, although insufficiently digested (more information provided in the text), are included to show how sample weight controls total recoveries. (b) The effect of atmospheric conditions on recoveries, where samples (i.e., supergene-altered Weld Range BIF and the collection of assorted global BIF) that were digested under both oxic (Method A) and inert (Method B) conditions are compared. Method A* indicates other (mostly hypogene-altered) Weld Range samples that were only digested under oxic conditions, for comparison. (c) Recoveries of the REE in sequential extractions were controlled by atomic number, where a higher atomic number resulted in better elemental recoveries.

2012; Viehmann et al., 2015a).

6.3.1. *Suitability of least-altered BIF to undertake paleo-environmental reconstructions*

The only preserved example of the least-altered BIF end-member (WR517) has whole rock signatures comparable to seawater, with low clastic contamination ($Al_2O_3 < 0.7$ wt%) and REE patterns that are similar to modern seawater (Fig. 4a; Alexander et al., 2009; Bau, 1993; Bau and Dulski, 1996; Bolhar et al., 2004; Planavsky et al., 2010). However, unlike modern seawater, WR517 lacks the large negative Ce anomaly and possesses a large positive Eu anomaly consistent with other Archean BIF (Alexander et al., 2009; Bau, 1993; Bau and Dulski, 1996; Bolhar et al., 2004; Planavsky et al., 2010). The Weld Range BIF has an inferred depositional age of ca. 2.7 Ga (Duuring et al., 2018; Duuring et al., 2020) with deposition occurring under anoxic conditions prior to the onset of the GOE (~2.4 Ga; Gumsley et al., 2017), consistent with the absence of negative Ce anomalies in the samples. Cerium anomalies in BIF are controlled by oceanic oxygenation, where increasing oxygenation results in larger negative Ce anomalies (as exhibited in Phanerozoic seawater) due the oxidation of Ce^{3+} to Ce^{4+} and precipitation onto Mn (oxy)hydroxides, causing residual seawater to be significantly depleted in Ce relative to other REE (German and Elderfield, 1990; German et al., 1991; Wallace et al., 2017; Zhang and Shields, 2022). Therefore, due to redox controls on Ce anomalies, the presence or absence of Ce anomalies in post-GOE BIF are reflective of their depositional environments relative to the redoxcline/chemocline (i.e., the ca. 2.38–2.21 Ga Yuanjiacun BIF, China; Wang et al., 2015). However, some BIF occurrence prior to the GOE demonstrated possible large-scale oxygenation of oceans prior to the GOE, such as the Bababudan Group, India (2.9–2.7 Ga; Kato et al., 2002) and the Itabira IF, Brazil (2.65 Ga; Cabral et al., 2016), suggesting that seawater columns were not entirely anoxic (Kato et al., 2006) or that samples have undergone secondary modification. Note that the lack of negative Ce anomalies from other pre-GOE BIF occurrences, such as the Hamersley Basin BIF, Australia (ca. 2.6–2.4 Ga) or Transvaal BIF, South Africa (ca. 2.5 Ga), has been attributed to anoxia of land-locked oceans by hydrothermal activity (Kato et al., 2006; Ohmoto et al., 2006). Similar processes can explain the absence of Ce anomalies from the Weld Range BIF, given the presence of large positive Eu anomalies consistent with significant hydrothermal inputs into the REE seawater budget (Derry and Jacobsen, 1990; Ernst and Bau, 2021; Sylvestre et al., 2017; Viehmann et al., 2015a).

The ‘relatively’ low Y/Ho value of the least-altered WR517 (i.e., Y/Ho = 28.8), alongside the presence of positive La, Eu, Gd anomalies and relative $HREE_{SN}$ enrichment, suggests the influence of both ambient seawater and hydrothermal fluid. Low Y/Ho can be indicative of clastic contamination (Ernst and Bau, 2021; Sylvestre et al., 2017), but there is a poor correlation between Al_2O_3 and both REE and Zr in the Weld Range BIF (Fig. 6a,c). Therefore, similar to the Kouambo BIF, Cameroon (average Y/Ho value of 29.48; Sylvestre et al., 2017), the lower Y/Ho at Weld Range is consistent with high-temperature hydrothermal fluid influencing the seawater REE budget or equilibration with surrounding lithologies that have low Y/Ho ratios (Ernst and Bau, 2021; Sylvestre et al., 2017). However, based on trace element systematics, the influence of hydrothermal fluids is relatively minor (<0.01 % hydrothermal fluid; Fig. 10). Nevertheless, the least-altered Weld Range BIF contains negligible clastic contamination and is reflective of seawater-like characteristics, matching trends observed in the pristine IF-G, IF-WA, the Asbestos Hills BIF, and the Dales Gorge BIF (Fig. 10 and Fig. 11), thus, the least-altered Weld Range BIF is considered suitable for paleo-environmental reconstructions.

6.3.2. *Potential of using hypogene- and supergene-altered BIF for paleo-environmental reconstructions*

Hypogene- and supergene-altered Weld Range BIF display numerous characteristics that reflect seawater-like signatures, comparable to the least-altered BIF, such as $HREE_{SN}$ enrichment, positive La, Eu, Gd and Y anomalies (Table 4; Fig. 4). Hypogene-altered samples also possess higher Y/Ho ratios (mean = 36.6; n = 11). When higher Y/Ho ratios are observed in pristine BIF this indicates a lower magmatic-hydrothermal influence (Bau and Dulski, 1996; Sylvestre et al., 2017). However, in the case of intensely hypogene-altered BIF, higher Y/Ho ratios are more likely a function of post-deposition fluids and/or relative mineral proportions, with these samples typically containing higher proportions of silicates and carbonates and lower proportions of Fe oxides relative to least-altered WR517 (Table 3). Numerous studies have indicated preferential scavenging of Ho (and other REE) relative to Y by Fe-(oxy)

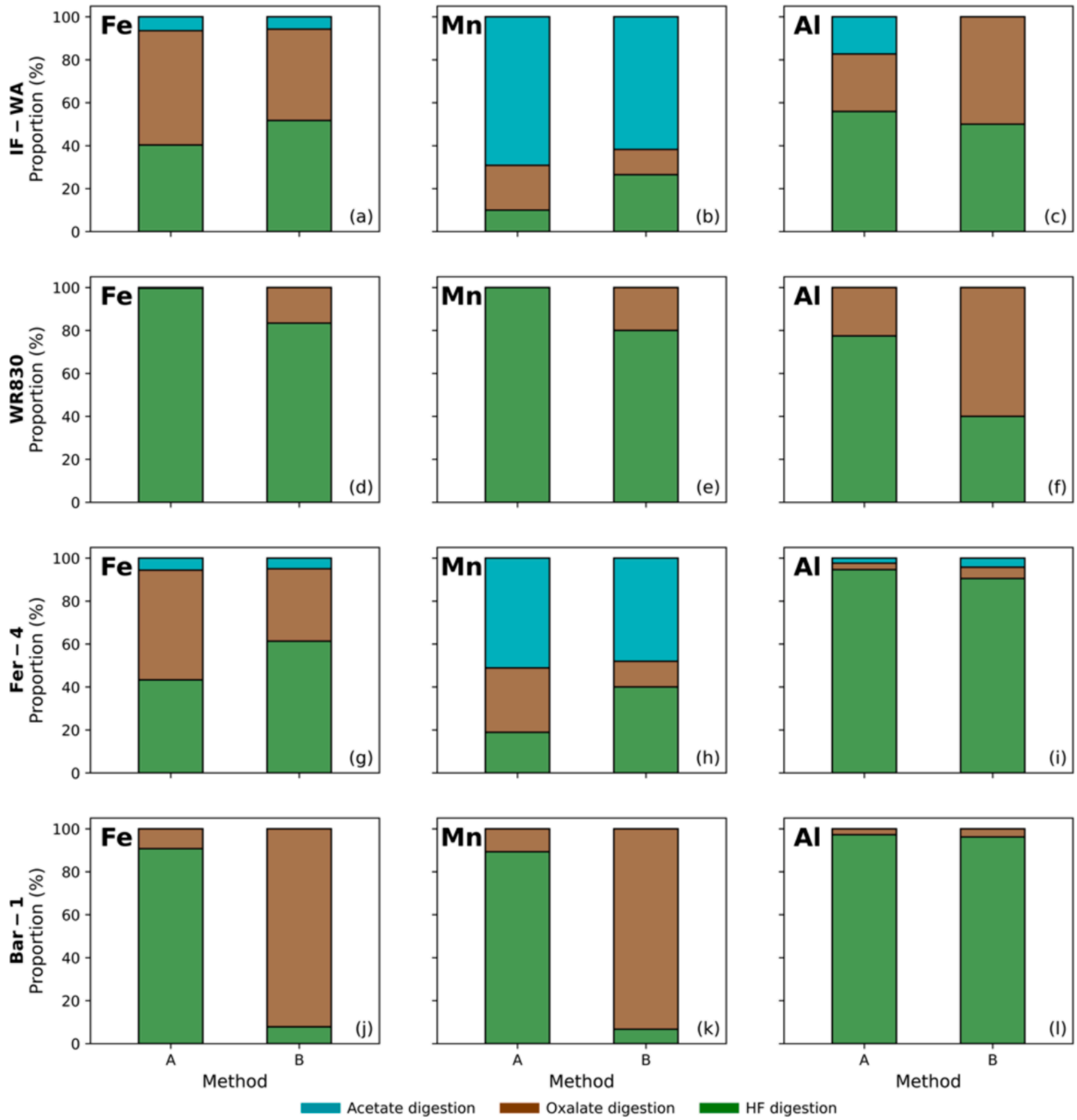

Fig. 9. Normalised proportions (i.e. to 100%) of total amount of Fe, Mn, and Al recovered from each of the acetate (carbonate), oxalate (Fe oxide) and HF (silicate) fractions from BIF of variable mineralogy. (a-c) pristine IF-WA; (d-f) supergene-altered WR830 and (g-i) reference material Fer-4; and (j-l) supergene-altered Bar-1. For magnetite-rich samples IF-WA and Fer-4 inert conditions for Fe oxide digestion (Method B) resulted in recoveries and mineral proportions that were within the margin of error relative to traditionally used oxic conditions (Method A). However, inert conditions (Method B) resulted in improved oxalate digestions of Fe oxides in magnetite-absent supergene-altered WR830 and Bar-1, whereas oxic conditions (Method A) resulted in incomplete digestion.

hydroxides during BIF and Fe-Mn crust formation, resulting in lower Y/Ho ratios in Fe oxides relative to seawater where precipitation is rapid and exchange equilibrium has not been reached (Bau, 1999; Bau and Dulski, 1996; Bau and Koschinsky, 2009; Bau et al., 1996; Bau et al., 2014; Ernst and Bau, 2021). Previous studies (e.g., Rasmussen et al., 2013; Rasmussen et al., 2017) suggest that variable Y/Ho between bands can indicate post-depositional separation through diagenesis of Fe-rich and Si-rich bands from a primary Fe-silicate ooze. However, Ernst and Bau (2021) showed uniform Y/Ho in the Fe oxide and metachert bands from the Mt. Ruker BIF, Antarctica, indicating, alongside variable Eu anomalies between bands, that banding is primary and not facilitated by post-depositional processes. However, variable Y/Ho is observed between Fe-rich and Si-rich bands in BIF from the Pongola Supergroup, South Africa (Delvigne et al., 2012), and between magnetite and grunerite in the Badampahar BIF, India, and Nuvvuagittuq BIF, Canada (Ghosh, 2020). Therefore, it is possible that primary deposition of

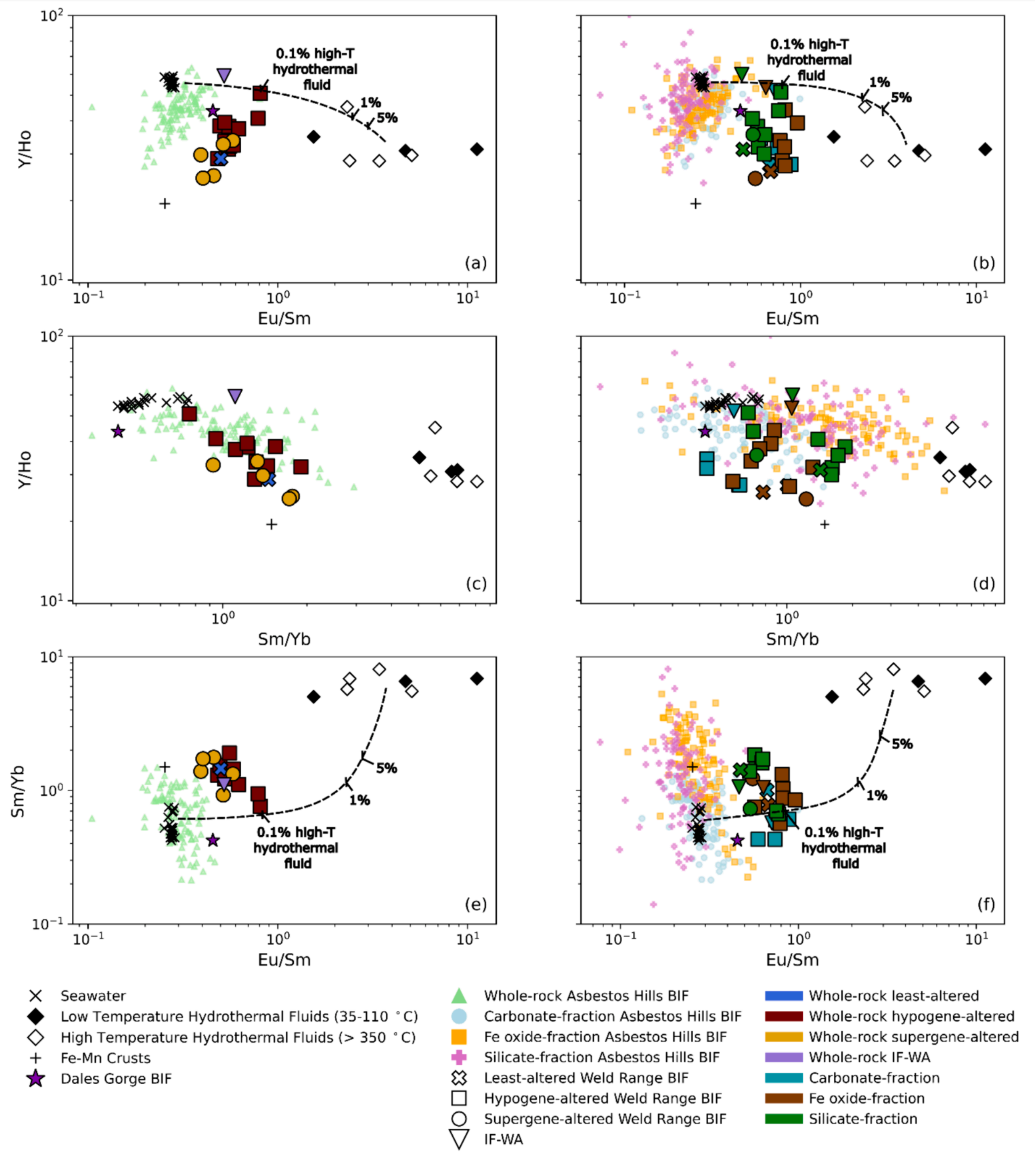

Fig. 10. Whole-rock and fraction-specific assessment of hydrothermal influence using mixing models of Y/Ho vs Eu/Sm (a, b), Y/Ho vs Sm/Yb (c, d), and Sm/Yb vs Eu/Sm (e, f), respectively (Alexander et al., 2008). These graphs suggest possible preservation of seawater chemistry and little to no influence by hydrothermal fluids. Data from the Asbestos Hills BIF (Oonk et al., 2018; Oonk et al., 2017), Dales Gorge BIF (Pecoits et al., 2009), seawater (Alibo and Nozaki, 1999), Fe-Mn crust (averaged from Wen et al., 1997), and hydrothermal fluids (Bau and Dulski, 1999) are used for comparison.

carbonates, Fe oxides, and silicates, can facilitate non-uniform Y-Ho fractionation. This is also the case in hypogene-altered Weld Range BIF where dissolution of Fe oxides, or precipitation of secondary carbonates and Fe oxides, may alter whole-rock Y/Ho ratios. However, at Weld Range, the hypogene alteration fluids are comparable to Archean seawater (Duuring et al., 2018), consequently the Y/Ho ratios of hypogene minerals are comparable to pristine minerals. Therefore, higher Y/Ho ratios with progressive hypogene alteration as exhibited by Weld Range are proposed to be a function of mineral proportion variability (i.e., lower proportions of Fe oxides relative to carbonates and silicates) rather than variable Y/Ho ratios of the alteration fluids through time.

Supergene-altered samples, on the other hand, possess lower Y/Ho that are similar to least-altered BIF (mean = 29.0; n = 5). Lower Y/Ho ratios in the supergene-altered samples may reflect Y/Ho ratios of supergene alteration fluids due to possible open-system interaction with surrounding lithologies and high water/rock ratios (Duuring and Hagemann, 2013a; Duuring and Hagemann, 2013b), and higher proportions of Fe-rich minerals (hematite and goethite, specifically) and dissolution of carbonates and silicates. The same phenomena (i.e., relatively low Y/Ho ratios) was observed in weathered BIF from the

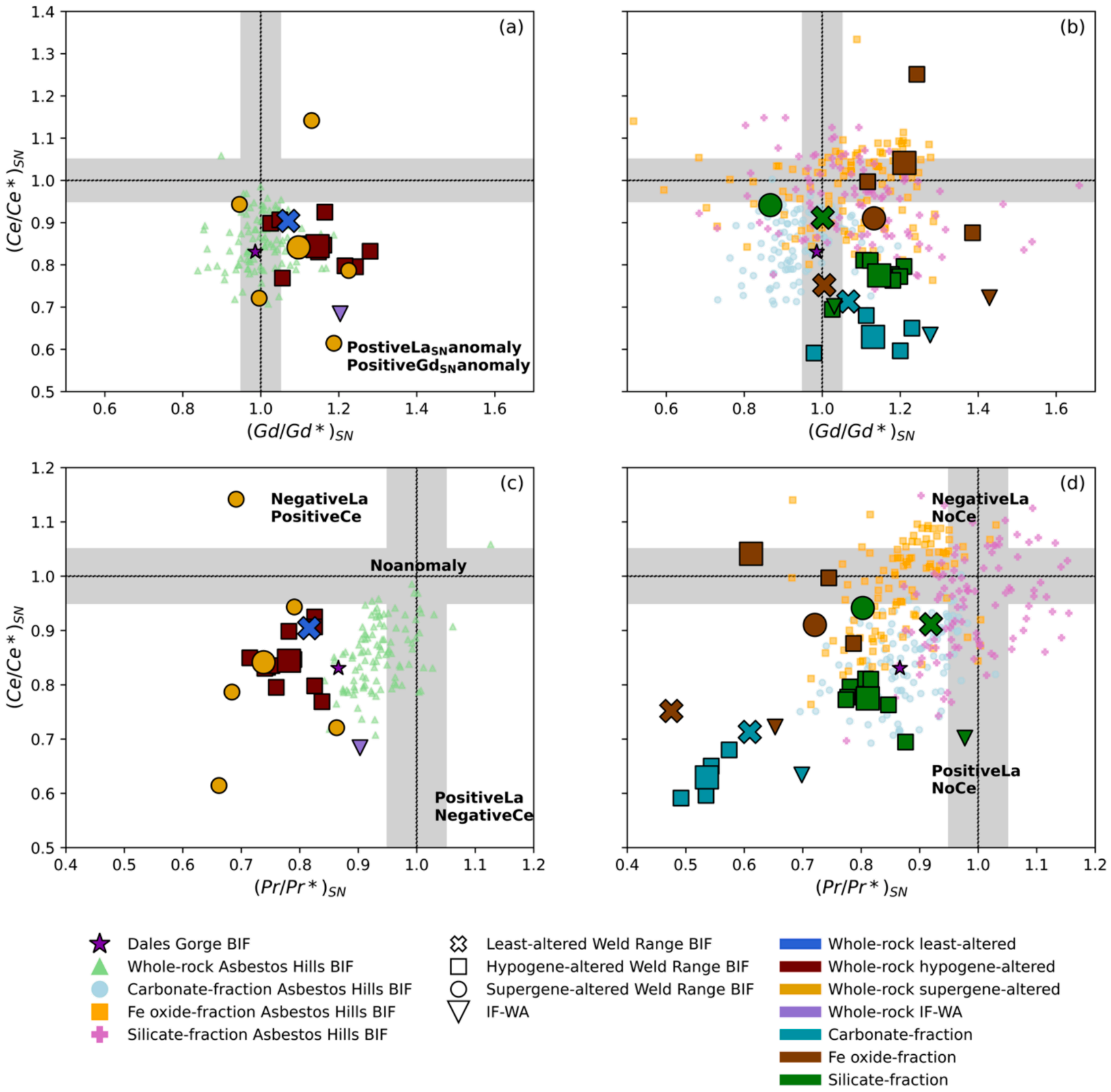

Fig. 11. Assessment of REE anomalies in whole-rock and fraction-specific Weld Range BIF (Alexander et al., 2008; Bau and Dulski, 1996). Whole-rock $(Ce/Ce^*)_{SN}$ vs $(Gd/Gd^*)_{SN}$ and $(Ce/Ce^*)_{SN}$ vs $(Pr/Pr^*)_{SN}$ graphs (a and c, respectively) suggest seawater-like signatures across least-altered and altered Weld Range BIF due to similarity with the Dales Gorge (Pecoits et al., 2009) and the pristine Asbestos Hills BIF (Oonk et al., 2018; Oonk et al., 2017). Fraction-specific graphs (b and d) suggest that the silicate-fraction more closely aligns with signatures from the pristine Dales Gorge BIF and Asbestos Hills BIF and thus serves as a more robust proxy for paleo-environmental reconstructions of altered Weld Range BIF.

Hamersley Basin, Australia (Li et al., 2023). Therefore, depositional environment, post-depositional events and whole-rock mineral proportions can strongly influence Y/Ho, and potentially other ratios and anomalies used to discern seawater characteristics, highlighting the importance of undertaking mineral fraction-specific studies for paleo-environmental reconstructions of both pristine and altered BIF.

Nickel and Zn concentrations are variable across hypogene- and supergene-altered Weld Range samples, indicating post-depositional elemental addition by alteration fluids (Fig. 7c). Nickel and Zn were selected based on a systematic study of the alteration fluids at Weld Range (Duuring et al., 2018), where increasing concentrations of these elements indicates increased magmatic influence in the fluids. Variability of Ni and Zn will also be controlled by changes in the composition of the hypogene alteration fluids (i.e., changing mixtures of magmatic-derived fluid and Archean seawater through time). Therefore, although the whole-rock hypogene- and supergene-altered Weld Range samples exhibit seawater-like characteristics in some instances, these are a consequence of their secondary paragenesis rather than primary BIF deposition, and untangling these signatures is extremely complex.

6.3.3. *Correlations between REE and mobile and immobile elements*

The influence of clastic contamination and post-depositional mobility in whole-rock (and fraction-specific) BIF compositions can be determined through correlation coefficients between elements. For example, Alexander et al. (2009) argued against significant post-depositional mobility in BIF from the Pietersburg greenstone belt, South Africa, due to strong correlations between Ti and both mobile and immobile elements (e.g. Rb, Ni, Th and Co). However, strong positive correlations between immobile elements (i.e., Ti and Th) may also indicate possible clastic contamination, especially at concentrations higher than the ‘cut-offs’ for those elements (e.g., 5 ppm ’cut-off’ for Zr; Basta et al., 2011; Bau, 1993; Djoukouo Soh et al., 2021; Ernst and Bau, 2021; Pecoits et al., 2009).

For the Weld Range BIF, correlation coefficients have been calculated between REE and both mobile (Rb, Sr, Ca, Ba, U) and immobile (Ti, Zr, Nb, Hf, Th; Fig. 12) elements to determine the controls on REE signatures and whether they reflect primary seawater chemistry. Supergene-altered samples were omitted from these calculations due to the secondary disturbance of all mineral fractions remaining in the samples (i.e., complete removal of carbonates and replacement of primary/hypogene Fe oxides and silicates with supergene counterparts; Table 1). Including these samples in correlation coefficient calculations would have distorted the dataset based on signatures generated completely from secondary overprinting.

Combined correlation coefficients for the least- and hypogene-altered Weld Range samples in the whole-rock show moderate correlation ($r^2 = \sim 0.6$) between REE and immobile elements (Ti, Zr, Nb, Hf, Th), suggesting some minor influence of clastic contamination on immobile element concentrations. However, poor correlations between whole-rock Zr and Al_2O_3, and the overall low Al_2O_3 concentrations of (<0.7 wt%) rebut any significant clastic contamination in the Weld Range BIF. Nevertheless, whole-rock correlation coefficients are strongly controlled by the elemental correlations of the different major mineral fractions, as indicated by variable r^2 values, where some mineral fractions in the Weld Range BIF are more prone to elemental disturbance by alteration events than others. For example, according to the alteration assemblages of BIF from the Beebyn and Madoonga deposits (Table 1), carbonate minerals are mostly secondary to the system whereas silicate minerals are predominantly primary. Therefore, the abundance of primary and secondary minerals coupled with the relative mineral fraction proportions in a specific sample will control the whole-rock signatures. For example, correlation coefficients from the comparative pristine Asbestos Hills BIF (Oonk et al., 2018; Oonk et al., 2017) strongly mimic signatures observed in the silicate-fraction

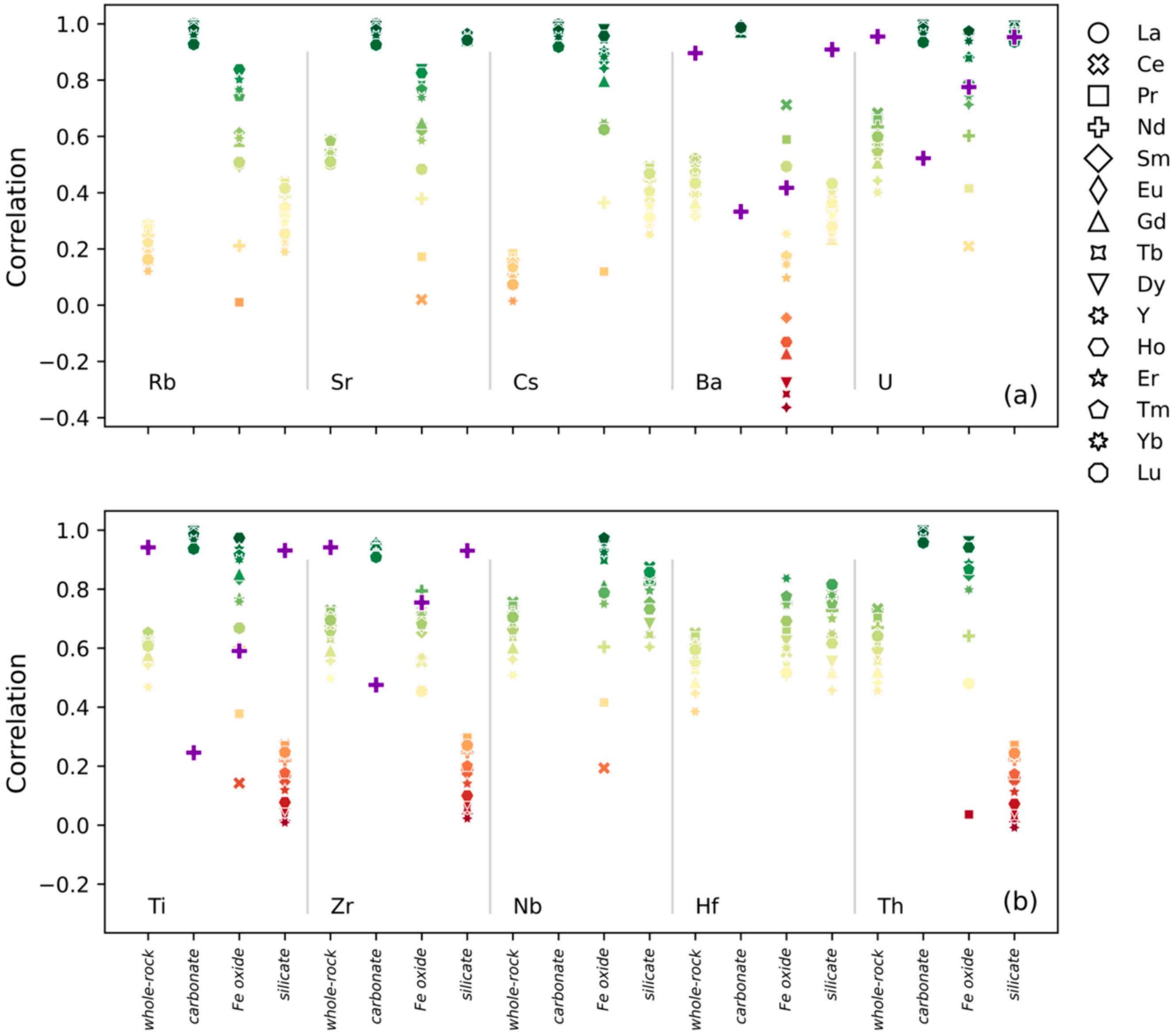

Fig. 12. Correlation covariance of mobile (a) and immobile (b) elements relative to REE for the different BIF fractions considered (i.e. whole-rock, carbonate-, Fe oxide-, and silicate-fractions). Covariance was calculated using only least-altered and hypogene altered Weld Range samples (n = 14). Correlation covariances for Hf in the carbonate-fraction are excluded due to Hf concentration below the detection limit. Correlation covariances with Nd calculated from the Asbestos Hills BIF are included in the graphs as purple crosses (Oonk et al., 2018; Oonk et al., 2017). The silicate-fraction in the Weld Range BIF most closely aligns with correlation covariance of the carbonate-fraction in the Asbestos Hills BIF, which is suggested to reflect pristine seawater signatures. Whereas, the carbonate-fraction of the Weld Range BIF closely aligns with the silicate-fraction in the Asbestos Hills BIF, suggesting secondary and/or clastic influences.

(Fig. 12), due the silicate-fraction consisting of ~ 57 % of the whole rock on average across the sample suite. Consequently, determining the influence of clastic contamination in whole-rock samples through correlation coefficients is not appropriate where mineral fractions (i.e., carbonate-, Fe oxide- and silicate-fractions) have been affected differently. Similarly, the correlations between whole-rock REE and mobile elements (Rb, Sr, Cs, Ba, U; Fig. 12) provides restricted insight into the systematics that affected the individual mineral fractions during post-depositional processes, such as diagenesis and hypogene alteration events and therefore the systematics of individual mineral fractions will be discussed below, to determine the most suitable mineralogical fraction (if any) for reconstructing primary oceanic signatures.

6.4. Interrogating fraction-specific paleo-environmental reconstructions from the Weld Range BIF

Fraction-specific analyses (such as those undertaken in Ernst and Bau, 2021; Gourcerol et al., 2016; Gourcerol et al., 2015; Oonk et al., 2018; Oonk et al., 2017) provide insights into the depositional and post-depositional systematics for each individual mineral fraction (i.e., carbonate-, Fe oxide- and silicate-fraction). For example, fraction-specific analysis on the pristine Asbestos Hills BIF determined that the carbonate-fraction most closely resembles seawater signatures, whereas Fe oxide- and silicate-fractions were highly variable and reflect diagenetic and clastic contamination controls (Oonk et al., 2018). Similar to whole-rock systematics, mineral fractions from the least- and hypogene-altered Weld Range BIF generally reflected seawater characteristics through the preservation of $\mathrm{HREE_{SN}}$ enrichment relative to $\mathrm{LREE_{SN}}$, and positive La, Eu, Gd, and Y anomalies.

6.4.1. Carbonate-fraction

The carbonate-fraction of the least-altered end-member WR517, relative to the whole-rock data, demonstrated slightly lower $\mathrm{Nd/Yb_{SN}}$ (whole-rock (WR) = 0.48, carbonate-fraction (carb) = 0.26), Y/Ho (WR=28.8, carb = 27.2), $\mathrm{Y/Y^{*}_{SN}}$ (WR=1.14, carb = 1.09), and higher $\mathrm{Eu/Eu^{*}_{SN}}$ values (WR=2.53, carb = 3.10). These slight differences in values indicate a slightly larger influence from high-temperature hydrothermal fluids (<0.1 %) in the deposition of the least-altered carbonate-fraction, relative to the whole-rock. Similar characteristics are observed across the carbonate-fractions of hypogene-altered samples (i.e., slightly lower $\mathrm{Nd_{SN}/Yb_{SN}}$, Y/Ho, and $\mathrm{Y/Y^{*}_{SN}}$ values, and slightly higher $\mathrm{Eu/Eu^{*}_{SN}}$ values; Fig. 4). In pristine BIF, Fe-rich carbonates, such as ankerite and siderite (which are observed in the Weld Range BIF), can precipitate due to equilibration of $\mathrm{Fe^{2+}}$ with dissolved inorganic carbon in seawater, or through diagenesis or dissimilatory iron reduction (Heimann et al., 2010; Johnson et al., 2008; Köhler et al., 2013; Pecoits et al., 2009; Wang et al., 2015). Nevertheless, Fe-rich carbonate precipitation depends on the presence of $\mathrm{Fe^{2+}/Fe^{3+}}$ in seawater, facilitating deposition during hydrothermal flux events (Bolhar et al., 2005b; Jiang et al., 2022; Steinhoefel et al., 2009; Van Kranendonk et al., 2003) as indicated by $\mathrm{Nd/Yb_{SN}}$, Y/Ho and Y and Eu anomaly values. Iron-controlled precipitation of Fe-rich carbonates also likely resulted in similar scavenging properties as Fe-(oxy)hydroxides, where Ho is preferentially scavenged relative to Y, causing lower Y/Ho ratios and positive Y anomalies where precipitation is rapid (i.e., exchange equilibrium is not acheived; Bau, 1999; Bau and Dulski, 1996; Bau and Koschinsky, 2009; Bau et al., 1996; Bau et al., 2014; Ernst and Bau, 2021). However, the carbonate-fraction of the hypogene-altered Weld Range BIF had a slightly greater magmatic-hydrothermal influence due to carbonate precipitation from hypogene alteration events (Fig. 7). Based on the alteration assemblages of the Beebyn and Madoonga deposits (Table 1), carbonate minerals are secondary to the system and are the product of hypogene alteration. The hypogene alteration fluids at Weld Range have a magmatic origin with an Archean seawater mixing component (e.g., Duuring et al., 2018), resulting in slightly more prevalent hydrothermal signatures (i.e., lower Y/Ho and higher Eu anomalies) whilst still preserving secondary seawater characteristics. As a result, the carbonate fraction in the hypogene-altered BIF is reflective of hypogene alteration fluids rather than primary seawater signatures. The carbonate-fraction of the least-altered WR517 should also be interpreted with caution, as it only constitutes a small proportion of the total sample (~5 %) and likely reflects minor secondary mineral addition as it is not mentioned in the primary paragenesis determined in previous studies (Table 1; Duuring and Hagemann, 2013a; Duuring and Hagemann, 2013b). Therefore, it is not recommended to focus on the carbonate-fraction of the Weld Range BIF for paleo-environmental reconstruction purposes.

6.4.2. Fe oxide-fraction

The Fe oxide-fraction of the least-altered BIF reflects a slightly greater hydrothermal influence than the carbonate fraction due to slightly lower $\mathrm{Nd/Yb_{SN}}$, Y/Ho, and $\mathrm{Y/Y^{*}_{SN}}$ values, and slightly higher $\mathrm{Eu/Eu^{*}_{SN}}$ values (Supplementary Material Table S6). The slight lower Y/Ho ratios are attributed to preferential scavenging of Ho, relative to Y, by Fe-(oxy)hydroxides (Bau, 1999; Bau and Koschinsky, 2009; Bau et al., 1996; Bau et al., 2014). This is prominent during increased hydrothermal flux events that drive accumulation and oxidation of $\mathrm{Fe^{2+}}$ to $\mathrm{Fe^{3+}}$ in the Archean oceans (and subsequent Fe-(oxy)hydroxides; Bekker et al., 2010; Dodd et al., 2022; Ghosh, 2020; Thibon et al., 2019). The Fe oxide-fraction of the least-altered Weld Range BIF could thus potentially provide insights regarding episodic Fe precipitation, related to hydrothermal flux events. Similar to the Fe oxide-fraction within the pristine Asbestos Hills BIF (Oonk et al., 2018; Oonk et al., 2017), LREE concentrations in the Weld Range Fe oxide-fraction are very low (i.e., La ≤ 0.55 ppm; Pr ≤ 0.27 ppm). These very low LREE concentrations contribute to detection limit problems and mean that the Fe oxide-fraction is more susceptible to clastic contamination and hydrothermal influences (Table 5). Therefore, the Fe oxide-fraction of the least-altered Weld Range BIF is not considered ideal for paleo-environmental reconstructions.

Interestingly, the hypogene-altered samples have a less significant magmatic-hydrothermal influence across the Fe oxide-fraction than expected (Fig. 10). This signature must be a product of both primary signatures and secondary element addition, where primary Fe oxides remain preserved alongside newly precipitated secondary Fe oxides following hypogene alteration events (Duuring and Hagemann, 2013a; Duuring and Hagemann, 2013b; Duuring et al., 2018). During the later stages of hypogene alteration (e.g., Stages 3–7 at the Beebyn deposit) more extensive Fe oxide replacement occurred, with these stages representing lower temperature fluids with a greater contribution from Archean seawater (Duuring et al., 2018). Thus, despite the lower Y/Ho observed in the Fe oxide-fraction of the hypogene samples, which are similar to those typically observed in the Fe-rich bands or fractions in pristine BIF (e.g., Delvigne et al., 2012; Ghosh, 2020), this is a function of the higher Archean seawater component in the hypogene alteration fluid. Therefore, due to significant overprinting of the Fe oxide-fraction in hypogene-altered Weld Range BIF this fraction is not considered suitable for paleo-environmental reconstructions.

6.4.3. Silicate-fraction

The silicate-fraction of the least-altered Weld Range BIF exhibits numerous seawater characteristics, including $\mathrm{HREE_{SN}}$ enrichment, positive La, Eu, Gd, and Y anomalies, and slightly higher Y/Ho. Overall, the silicate-fraction appears more reflective of seawater than hydrothermal input, relative to the whole-rock and carbonate- and Fe oxide-fractions, due to slightly higher $\mathrm{Nd/Yb_{SN}}$ and Y/Ho and more positive Y anomalies (Fig. 10; Table 4). These subtle differences are due to the episodic deposition of Si-rich bands in BIF that occurs when hydrothermal activity has subsided (Bolhar et al., 2005b; Ghosh, 2020; Morris, 1993), possibly resulting in more representative primary seawater signatures. The counterpoint to this advantage is that the silicate-fraction is more likely to contain a greater proportion of clastic contamination (e.g., Oonk et al., 2018), due to the absence of hydrothermal flux, which typically dilutes the influence of clastic input. Nevertheless, the silicate-fraction of the least-altered Weld Range BIF appears to have minimal clastic input of Al-bearing minerals, based on the low Al_2O_3 content of 1.42 wt% (compared to up to 6.76 wt% Al_2O_3 in the clastic contaminated silicate-fraction from the Asbestos Hills BIF; Oonk et al., 2018; Oonk et al., 2017) and higher Y/Ho ratios and positive Y anomalies consistent with other pristine BIF (Bau and Dulski, 1996; Sylvestre et al., 2017). Several studies have suggested that higher Y/Ho may be an intrinsic characteristic of the silicate-fraction, with Si-rich bands or minerals from several global BIF locations (South Africa, India, Canada; Delvigne et al., 2012; Ghosh, 2020) exhibiting higher Y/Ho than Fe-rich bands or minerals. All things considered; we advocate that the silicate-fraction of the least-altered Weld Range BIF is the most suitable mineral fraction for determining primary Archean seawater chemistry.

Similarly, the silicate fraction of hypogene-altered BIF exhibits overall higher Y/Ho and Y anomalies, and lower Eu anomalies, relative to the carbonate- and Fe oxide-fractions, which is consistent with lower hydrothermal input and more ‘true’ seawater signatures (Fig. 10). This is also reflected by the lower Ni and Zn concentrations within the silicate-fraction, where the carbonate- and Fe oxide-fractions show increased Ni and Zn concentrations that are indicative of post-depositional elemental addition during the secondary precipitation of minerals by magmatic-derived fluids (Fig. 7d). The silicate-fraction of the hypogene-altered BIF also possesses HREE enrichment and positive La and Gd and Y anomalies (Fig. 5 and Fig. 11), which is characteristic of seawater. Unlike the carbonate- and Fe oxide-fractions, the silicate-fraction is predominantly primary and undisturbed in the Weld Range BIF, despite the intense and varied hypogene alteration (Table 1 and Table 3). As a result, the silicate-fraction within the hypogene-altered Weld Range BIF, which reflects negligible clastic contamination (i.e., < 1.42 wt% Al_2O_3) and preserves characteristics observed in seawater, and similar to the silicate-fraction of least-altered BIF. Therefore, the silicate-fraction, which is predominantly chert/quartz that has remained unaltered during post-depositional processes in the Weld Range samples is considered an appropriate mineralogical fraction for reconstructing primary Archean seawater signatures. However, this assessment will need to be made for each sample suite based on the petrogenetic history of the constituent mineral phases present.

6.4.4. *Correlations between REE and other elements in different mineralogical fractions*

Analogous to the whole-rock data, correlation coefficients were also calculated between REE and selected mobile and immobile elements, and compared to the pristine Asbestos Hills BIF (Oonk et al., 2018; Oonk et al., 2017), to determine the suitability of the different mineral fractions for reconstructing primary seawater chemistry. Correlation coefficients have only been calculated for the least- and hypogene-altered BIF samples that produced successful sequential extractions (i.e., each fraction represents the proportion of the rock expected from mineralogy and major element composition). The carbonate- and Fe oxides-fractions exhibit overall strong covariance between REE and immobile elements (i.e., Ti, Zr, and Th; Fig. 12b), whereas, the silicate-fraction predominantly shows poor correlations with these immobile elements, except for Nb and Hf which display moderate correlations (although the silicate fraction consistently has the lowest covariance). For comparison, fraction-specific data from the pristine Asbestos Hills BIF (Oonk et al., 2018; Oonk et al., 2017) were considered to aid interpretations. Correlations between the REE and Ti and Zr have weak-moderate correlations in the carbonate-fraction ($r^2 = 0.2$–0.5), moderate-strong correlations in the Fe oxide-fraction ($r^2 = 0.6$–0.8) and very strong correlations in the silicate-fraction ($r^2 = 0.9$). These correlations coefficients, alongside other interpretations in Oonk et al. (2018), suggest that in the Asbestos Hills BIF the carbonate-fraction most closely resembles seawater, whereas the Fe oxide- and silicate-fractions are more prone to clastic contamination and diagenetic influences. However, a different interpretation is required when analysing the individual mineral fractions from hypogene-altered Weld Range BIF. Strong covariance between the REE and immobile elements (e.g., Ti-Nd $r^2 = \sim 1$) in the carbonate-fraction and Fe oxide- fractions (e.g., Ti-Nd $r^2 = 0.6$; Fig. 12) suggested in both instances, but especially the carbonates, that these correlations are controlled by the precipitation of new minerals that have preserved the elemental systematics from the alteration fluids. Conversely, the weak correlation between immobile elements and REE in the silicate-fraction (e.g., Ti-Nd $r^2 = 0.2$; Fig. 12) is consistent with negligible influence from either alteration overprinting or clastic contamination in this fraction. Furthermore, the correlations coefficients between immobile elements (Ti and Zr) in the silicate-fraction from the Weld Range BIF are similar to those in what is considered the most pristine archive of seawater the carbonate-fraction of the Asbestos Hills BIF.

Similarly, offset characteristics between different mineral fraction in the Weld Range BIF and Asbestos Hills BIF are also observed when considering the covariance between the REE and mobile elements. For example, the mobile elements considered (Ba, Cs, Rb, Sr, U; Fig. 12b) exhibit very strong correlations ($r^2 = >0.9$) with the REE in the carbonate-fraction of the Weld Range BIF, consistent with this being inherited directly from the alteration fluid during secondary mineral precipitation. In contrast, poorer weak-moderate correlations (e.g., Nd-Cs $r^2 = 0.4$) are observed for the most incompatible and extremely fluid mobile elements (Ba, Cs, Rb; Fig. 12b) in the silicate-fraction of the Weld Range BIF, again these weak correlations are comparable to that observed in the pristine carbonate-fraction of the Asbestos Hills BIF for Ba. Interestingly, U and Sr are more difficult to interpret with both elements, exhibiting strong correlations with the REE in the silicate fraction, although this is probably merely a function of them being equally sourced from both crustal and oceanic reservoirs as the REE elements in the Weld Range BIF. Overall, elemental correlation systematics, combined with observations above, confirm that the silicate-fraction is the most accurate representation of pristine seawater available within the hypogene altered Weld Range BIF.

7. Conclusions

Based on a comprehensive whole-rock and fraction-specific study investigating major and trace element compositions of variably hypogene- and supergene-altered BIF from Weld Range, Yilgarn Craton, Western Australia the following has been discovered:

1. Sequential extractions on magnetite-poor BIF are complicated, and careful scrutinisation of recoveries and fraction purity is required. Future studies undertaking sequential extractions of hematite- and/or goethite-rich BIF should use inert conditions for the Fe-oxide digestion step to ensure complete digestion of the Fe-oxide fraction.
2. There are no geochemical indications of clastic contamination controlling the elemental signatures of the Weld Range BIF. This is supported by the low Al_2O_3 contents and lack of clear correlations between the REE and other clastic derived elements (e.g., Zr).
3. The least-, hypogene- and supergene-altered Weld Range BIF all possess signatures that are characteristic of seawater. These signatures included shale-normalised HREE enrichment, positive La, Eu, Gd and Y anomalies, and near- to super-chondritic Y/Ho ratios. However, whole-rock analysis, particularly for hypogene- and supergene-altered samples, is not appropriate for paleo-environmental reconstruction where minerals have been overprinted.
4. The carbonate- and Fe oxide-fractions of the hypogene-altered BIF, although indicative of seawater chemistry, are likely reflective of post-depositional overprinting. The preservation of seawater chemistry is attributed to a strong Archean seawater influence in the hypogene alteration fluids, which aided to the precipitation of secondary carbonate and Fe oxide minerals.

5. The silicate-fraction of the hypogene-altered Weld Range BIF is the most suitable reservoir for undertaking any paleo-environmental reconstructions. This is due to the primary nature of the mineral fraction throughout the sample suite (with little to no post-depositional overprinting), and is further supported by the distinctive seawater characteristics and correlation coefficients between REE and mobile and immobile elements which reinforce the undisturbed nature of the silicate fraction.

CRediT authorship contribution statement

Samantha C. Russo: Writing – original draft, Visualization, Validation, Methodology, Investigation. **Alex J. McCoy-West:** Writing – original draft, Visualization, Validation, Supervision, Methodology, Funding acquisition, Conceptualization. **Paul Duuring:** Writing – review & editing, Resources.

Declaration of competing interest

The authors declare that they have no known competing financial interests or personal relationships that could have appeared to influence the work reported in this paper.

Data availability

Provided in the supplementary material

Acknowledgements

Weld Range samples used in this study were made available by the Geological Survey of Western Australia. SCR acknowledges receipt of the EGRU Honours Scholarship, the AIG Student Honours Bursary, and an Australian Postgraduate PhD Scholarship to complete this work. AMW acknowledges ARC grant DE210101395. PD publishes with permission of the Director, Geological Survey of Western Australia. Yi Hu, Brendan Jones, Shane Askew at the Advanced Analytical Centre, JCU are thanked for technical assistance. Priyadarshi Chowdhury is graciously thanked for providing the Indian BIF samples. Paul Olin and Elena Lounejeva from Centre for Ore Deposits and Thomas Rodemann of the Central Science Laboratory at the University of Tasmania are thanked undertaking the analyses and providing details of analytical procedures. Mark Nestmeyer, Anne Kaufmann and Brandon Mahan are thanked for discussions at JCU. The reviewers and editors are thanked for their insight and comments.

Appendix A. Supplementary data

Supplementary data to this article can be found online at https://doi.org/10.1016/j.precamres.2024.107573.

References

Aftabi, A., Atapour, H., Mohseni, S., Babaki, A., 2021. Geochemical discrimination among different types of banded iron formations (BIFs): A comparative review. Ore Geol. Rev. 136, 104244.

Alexander, B.W., Bau, M., Andersson, P., Dulski, P., 2008. Continentally-derived solutes in shallow Archean seawater: Rare earth element and Nd isotope evidence in iron formation from the 2.9Ga Pongola Supergroup, South Africa. Geochim. Cosmochim. Acta 72 (2), 378–394.

Alexander, B.W., Bau, M., Andersson, P., 2009. Neodymium isotopes in Archean seawater and implications for the marine Nd cycle in Earth's early oceans. Earth Planet. Sci. Lett. 283 (1), 144–155.

Alibert, C., 2016. Rare earth elements in Hamersley BIF minerals. Geochim. Cosmochim. Acta 184, 311–328.

Alibert, C., McCulloch, M.T., 1993. Rare earth element and neodymium isotopic compositions of the banded iron-formations and associated shales from Hamersley, Western Australia. Geochimica et Cosmochimica Acta 57 (1), 187–204.

Alibo, D.S., Nozaki, Y., 1999. Rare earth elements in seawater: particle association, shale-normalization, and Ce oxidation. Geochim. Cosmochim. Acta 63 (3), 363–372.

Baker, J., Waight, T., Ulfbeck, D., 2002. Rapid and highly reproducible analysis of rare earth elements by multiple collector inductively coupled plasma mass spectrometry. Geochim. Cosmochim. Acta 66 (20), 3635–3646.

Baldwin, G.J., Turner, E.C., Kamber, B.S., 2012. A new depositional model for glaciogenic Neoproterozoic iron formation: insights from the chemostratigraphy and basin configuration of the Rapitan iron formation. Can. J. Earth Sci. 49 (2), 455–476.

Barany, S., Strelko, V., 2013. Laws and mechanism of adsorption of cations by different ion-exchange forms of silica gel. Adsorption 19 (2), 769–776.

Basta, F.F., Maurice, A.E., Fontboté, L., Favarger, P.-Y., 2011. Petrology and geochemistry of the banded iron formation (BIF) of Wadi Karim and Um Anab, Eastern Desert, Egypt: Implications for the origin of Neoproterozoic BIF. Precambr. Res. 187 (3), 277–292.

Basu, P., Ishwar-Kumar, C., Chaudhary, S., Chakrabarti, R., Satish-Kumar, M., Sajeev, K., 2022. Major, trace element, and Nd isotopic compositions of banded iron formation and shales from the Sirsi shelf, Dharwar Craton, India: Implications for paleo-seawater chemistry, post-depositional alteration, and provenance. Precambr. Res. 382, 106882.

Bau, M., 1991. Rare-earth element mobility during hydrothermal and metamorphic fluid-rock interaction and the significance of the oxidation state of europium. Chem. Geol. 93 (3), 219–230.

Bau, M., 1993. Effects of syn- and post-depositional processes on the rare-earth element distribution in Precambrian iron-formations. Eur. J. Mineral. 5 (2), 257–267.

Bau, M., 1999. Scavenging of dissolved yttrium and rare earths by precipitating iron oxyhydroxide: experimental evidence for Ce oxidation, Y-Ho fractionation, and lanthanide tetrad effect. Geochim. Cosmochim. Acta 63 (1), 67–77.

Bau, M., Alexander, B.W., 2009. Distribution of high field strength elements (Y, Zr, REE, Hf, Ta, Th, U) in adjacent magnetite and chert bands and in reference standards FeR-3 and FeR-4 from the Temagami iron-formation, Canada, and the redox level of the Neoarchean ocean. Precambr. Res. 174 (3), 337–346.

Bau, M., Dulski, P., 1992. Small-scale variations of the rare-earth element distribution in Precambrian iron-formations. Eur. J. Mineral. 4 (6), 1429–1433.

Bau, M., Dulski, P., 1996. Distribution of yttrium and rare-earth elements in the Penge and Kuruman iron-formations, Transvaal Supergroup. South Africa. Precambrian Research 79 (1), 37–55.

Bau, M., Dulski, P., 1999. Comparing yttrium and rare earths in hydrothermal fluids from the Mid-Atlantic Ridge: implications for Y and REE behaviour during near-vent mixing and for the Y/Ho ratio of Proterozoic seawater. Chem. Geol. 155 (1–2), 77–90.

Bau, M., Koschinsky, A., 2009. Oxidative scavenging of cerium on hydrous Fe oxide: evidence from the distribution of rare earth elements and yttrium between Fe oxides and Mn oxides in hydrogenetic ferromanganese crusts. Geochem. J. 43 (1), 37–47.

Bau, M., Koschinsky, A., Dulski, P., Hein, J.R., 1996. Comparison of the partitioning behaviours of yttrium, rare earth elements, and titanium between hydrogenetic marine ferromanganese crusts and seawater. Geochim. Cosmochim. Acta 60 (10), 1709–1725.

Bau, M., Möller, P., 1993. Rare earth element systematics of the chemically precipitated component in early precambrian iron formations and the evolution of the terrestrial atmosphere-hydrosphere-lithosphere system. Geochim. Cosmochim. Acta 57 (10), 2239–2249.

Bau, M., Schmidt, K., Koschinsky, A., Hein, J., Kuhn, T., Usui, A., 2014. Discriminating between different genetic types of marine ferro-manganese crusts and nodules based on rare earth elements and yttrium. Chem. Geol. 381, 1–9.

Bekker, A., Slack, J.F., Planavsky, N., Krapež, B., Hofmann, A., Konhauser, K.O., Rouxel, O.J., 2010. Iron Formation: The Sedimentary Product of a Complex Interplay among Mantle, Tectonic, Oceanic, and Biospheric Processes*. Econ. Geol. 105 (3), 467–508.

Beukes, N.J., Klein, C., Kaufman, A.J., Hayes, J.M., 1990. Carbonate petrography, kerogen distribution, and carbon and oxygen isotope variations in an early Proterozoic transition from limestone to iron-formation deposition, Transvaal Supergroup, South Africa. Econ. Geol. 85 (4), 663–690.

Bolhar, R., Kamber, B.S., Moorbath, S., Fedo, C.M., Whitehouse, M.J., 2004. Characterisation of early Archaean chemical sediments by trace element signatures. Earth Planet. Sci. Lett. 222 (1), 43–60.

Bolhar, R., Kamber, B.S., Moorbath, S., Whitehouse, M.J., Collerson, K.D., 2005a. Chemical characterization of earth's most ancient clastic metasediments from the Isua Greenstone Belt, southern West Greenland. Geochim. Cosmochim. Acta 69 (6), 1555–1573.

Bolhar, R., Van Kranendonk, M.J., Kamber, B.S., 2005b. A trace element study of siderite–jasper banded iron formation in the 3.45Ga Warrawoona Group, Pilbara Craton—Formation from hydrothermal fluids and shallow seawater. Precambr. Res. 137 (1), 93–114.

Bonnand, P., Lalonde, S., Boyet, M., Heubeck, C., Homann, M., Nonnotte, P., Foster, I., Konhauser, K., Köhler, I., 2020. Post-depositional REE mobility in a Paleoarchean banded iron formation revealed by La-Ce geochronology: A cautionary tale for signals of ancient oxygenation. Earth Planet. Sci. Lett. 547, 116452.

Cabral, A.R., Lehmann, B., Gomes, A.A.S., Pašava, J., 2016. Episodic negative anomalies of cerium at the depositional onset of the 2.65-Ga Itabira iron formation, Quadrilátero Ferrífero of Minas Gerais. Brazil. Precambrian Research 276, 101–109.

Cairns-Smith, A.G., 1978. Precambrian solution photochemistry, inverse segregation, and banded iron formations. Nature 276 (5690), 807–808.

Cameron, E.M., Baumann, A., 1972. Carbonate sedimentation during the Archean. Chem. Geol. 10 (1), 17–30.

Cloud, P., 1973. Paleoecological Significance of the Banded Iron-Formation. Econ. Geol. 68 (7), 1135–1143.

Currie, H., Perry, C., 2008. Silica in Plants: Biological, Biochemical and Chemical Studies. Ann. Bot. 100, 1383–1389.

Deer, W.A., Howie, R.A., Zussman, J., 1966. An introduction to the rock-forming minerals. Mineralogical Society of Great Britain and Ireland.

Delvigne, C., Cardinal, D., Hofmann, A. and André, L., 2012. Combining stratigraphic changes of Ge/Si, REE+ Y and silicon isotopes as insights into the deposition of a Mesoarchaean banded iron formation.

Derry, L.A., Jacobsen, S.B., 1990. The chemical evolution of Precambrian seawater: evidence from REEs in banded iron formations. Geochim. Cosmochim. Acta 54 (11), 2965–2977.

Djoukouo Soh, A.P., Ganno, S., Zhang, L., Soh Tamehe, L., Wang, C., Peng, Z., Tong, X., Nzenti, J.P., 2021. Origin, tectonic environment and age of the Bibole banded iron formations, northwestern Congo Craton, Cameroon: geochemical and geochronological constraints. Geol. Mag. 158 (12), 2245–2263.

Dodd, M.S., Wang, H., Li, C., Towner, M., Thomson, A.R., Slack, J.F., Wan, Y.-S., Pirajno, F., Manikyamba, C., Wang, Q., Papineau, D., 2022. Abiotic anoxic iron oxidation, formation of Archean banded iron formations, and the oxidation of early Earth. Earth Planet. Sci. Lett. 584, 117469.

Drever, J.I., 1974. Geochemical Model for the Origin of Precambrian Banded Iron Formations. GSA Bull. 85 (7), 1099–1106.

Duuring, P., Hagemann, S., 2013a. Genesis of superimposed hypogene and supergene Fe orebodies in BIF at the Madoonga deposit, Yilgarn Craton, Western Australia. Mineralium Deposita 48 (3), 371–395.

Duuring, P., Hagemann, S., 2013b. Leaching of silica bands and concentration of magnetite in Archean BIF by hypogene fluids: Beebyn Fe ore deposit, Yilgarn Craton, Western Australia. Mineralium Deposita 48 (3), 341–370.

Duuring, P., Hagemann, S.G., Banks, D.A., Schindler, C., 2018. A synvolcanic origin for magnetite-rich orebodies hosted by BIF in the Weld Range District, Western Australia. Ore Geol. Rev. 93, 211–254.

Duuring, P., Santos, J.O., Fielding, I.O., Ivanic, T.J., Hagemann, S.G., Angerer, T., Lu, Y.-J., Roberts, M., Choi, J., 2020. Dating hypogene iron mineralization events in Archean BIF at Weld Range, Western Australia: insights into the tectonomagmatic history of the northern margin of the Yilgarn Craton. Miner. Deposita 55, 1307–1332.

Ernst, D.M., Bau, M., 2021. Banded iron formation from Antarctica: The 2.5 Ga old Mt. Ruker BIF and the antiquity of lanthanide tetrad effect and super-chondritic Y/Ho ratio in seawater. Gondw. Res. 91, 97–111.

Fischer, W.W., Hemp, J., Johnson, J.E., 2016. Evolution of Oxygenic Photosynthesis. Annu. Rev. Earth Planet. Sci. 44 (1), 647–683.

Fischer, W.W., Knoll, A.H., 2009. An iron shuttle for deepwater silica in Late Archean and early Paleoproterozoic iron formation. GSA Bull. 121 (1–2), 222–235.

Garrels, R., Perry, E., Mackenzie, F., 1973. Genesis of Precambrian iron-formations and the development of atmospheric oxygen. Econ. Geol. 68 (7), 1173–1179.

German, C.R., Elderfield, H., 1990. Application of the Ce anomaly as a paleoredox indicator: The ground rules. Paleoceanography 5 (5), 823–833.

German, C.R., Holliday, B.P., Elderfield, H., 1991. Redox cycling of rare earth elements in the suboxic zone of the Black Sea. Geochim. Cosmochim. Acta 55 (12), 3553–3558.

Ghosh, R., 2020. Authigenic precipitation of ferric oxyhydroxides and greenalite in Archean oceans. Chem. Geol. 552, 119777.

Goldich, S.S., 1973. Ages of Precambrian banded iron-formations. Econ. Geol. 68 (7), 1126–1134.

Gole, M., 1980. Mineralogy and petrology of very-low-metamorphic grade Archaean banded iron-formations, Weld Range, Western Australia. American Mineralogist 65 (1–2), 8–25.

Gong, Q., Li, F., Lu, C., Wang, H., Tang, H., 2021. Tracing seawater- and terrestrial-sourced REE signatures in detritally contaminated, diagenetically altered carbonate rocks. Chem. Geol. 570, 120169.

Gourcerol, B., Thurston, P.C., Kontak, D.J., Côté-Mantha, O., 2015. Interpretations and implications of LA ICP-MS analysis of chert for the origin of geochemical signatures in banded iron formations (BIFs) from the Meadowbank gold deposit, Western Churchill Province, Nunavut. Chem. Geol. 410, 89–107.

Gourcerol, B., Kontak, D.J., Thurston, P.C., Duparc, Q., 2016. Do Magnetite Layers in Algoma-type Banded Iron Formations (bif) Preserve Their Primary Geochemical Signature? a Case Study of Samples from Three Archean Bif-hosted Gold Deposits. Can. Mineral. 54 (3), 605–624.

Gross, G.A., 1980. A classification of iron formations based on depositional environments. Can. Mineral. 18 (2), 215–222.

Gross, G.A., 1983. Tectonic systems and the deposition of iron-formation. Precambr. Res. 20 (2), 171–187.

Gross, G., 1990. Geochemistry of iron-formation in Canada. Ancient Banded Iron Formations. Regional presentations 3–26.

Gumsley, A.P., Chamberlain, K.R., Bleeker, W., Söderlund, U., De Kock, M.O., Larsson, E. R., Bekker, A., 2017. Timing and tempo of the Great Oxidation Event. Proc. Natl. Acad. Sci. 114 (8), 1811–1816.

Hagemann, S.G., Angerer, T., Duuring, P., Rosière, C.A., Figueiredo e Silva, R.C., Lobato, L., Hensler, A.S. and Walde, D.H.G., 2016. BIF-hosted iron mineral system: A review. Ore Geology Reviews, 76: 317-359.

Hamade, T., Konhauser, K.O., Raiswell, R., Goldsmith, S., Morris, R.C., 2003. Using Ge/Si ratios to decouple iron and silica fluxes in Precambrian banded iron formations. Geology 31 (1), 35–38.

Hartman, H., 1984. The evolution of photosynthesis and microbial mats: A speculation on the banded iron formations. MBL LECT, BIOL, p. 1984.

Haugaard, R., Frei, R., Stendal, H., Konhauser, K., 2013. Petrology and geochemistry of the ~2.9Ga Itilliarsuk banded iron formation and associated supracrustal rocks, West Greenland: Source characteristics and depositional environment. Precambr. Res. 229, 150–176.

Haugaard, R., Pecoits, E., Lalonde, S., Rouxel, O., Konhauser, K., 2016. The Joffre banded iron formation, Hamersley Group, Western Australia: Assessing the palaeoenvironment through detailed petrology and chemostratigraphy. Precambr. Res. 273, 12–37.

Heimann, A., Johnson, C.M., Beard, B.L., Valley, J.W., Roden, E.E., Spicuzza, M.J. and Beukes, N.J., 2010. Fe, C, and O isotope compositions of banded iron formation carbonates demonstrate a major role for dissimilatory iron reduction in ~2.5Ga marine environments. Earth and Planetary Science Letters, 294(1): 8-18.

Ho, M.D., Evans, G.J., 2000. Sequential Extraction of Metal Contaminated Soils with Radiochemical Assessment of Readsorption Effects. Environ. Sci. Tech. 34 (6), 1030–1035.

Holland, H.D., 1965. The history of ocean water and its effect on the chemistry of the atmosphere. Proc. Natl. Acad. Sci. 53 (6), 1173–1183.

Ingalls, M. and Snell, K.E., 2021. Tools for Comprehensive Assessment of Fluid-Mediated and Solid-State Alteration of Carbonates Used to Reconstruct Ancient Elevation and Environments. Frontiers in Earth Science, 9.

Jiang, C.Z., Halevy, I., Tosca, N.J., 2022. Kinetic isotope effect in siderite growth: Implications for the origin of banded iron formation siderite. Geochim. Cosmochim. Acta 322, 260–273.

Johnson, C.M., Beard, B.L., Klein, C., Beukes, N.J., Roden, E.E., 2008. Iron isotopes constrain biologic and abiologic processes in banded iron formation genesis. Geochim. Cosmochim. Acta 72 (1), 151–169.

Johnson, C.M., Ludois, J.M., Beard, B.L., Beukes, N.J., Heimann, A., 2013. Iron formation carbonates: Paleoceanographic proxy or recorder of microbial diagenesis? Geology 41 (11), 1147–1150.

Kato, Y., Kano, T. and Kunugiza, K., 2002. Negative Ce Anomaly in the Indian Banded Iron Formations: Evidence for the Emergence of Oxygenated Deep-Sea at 2.9-2.7 Ga. Resource Geology, 52(2): 101-110.

Kato, Y., Yamaguchi, K.E. and Ohmoto, H., 2006. Rare earth elements in Precambrian banded iron formations: Secular changes of Ce and Eu anomalies and evolution of atmospheric oxygen. In: S.E. Kesler and H. Ohmoto (Editors), Evolution of Early Earth's Atmosphere, Hydrosphere, and Biosphere - Constraints from Ore Deposits. Geological Society of America, pp. 0.

Klein, C., 2005. Some Precambrian banded iron-formations (BIFs) from around the world: Their age, geologic setting, mineralogy, metamorphism, geochemistry, and origins. Am. Mineral. 90 (10), 1473–1499.

Köhler, I., Konhauser, K.O., Papineau, D., Bekker, A., Kappler, A., 2013. Biological carbon precursor to diagenetic siderite with spherical structures in iron formations. Nat. Commun. 4 (1), 1741.

Konhauser, K.O., Amskold, L., Lalonde, S.V., Posth, N.R., Kappler, A., Anbar, A., 2007. Decoupling photochemical Fe(II) oxidation from shallow-water BIF deposition. Earth Planet. Sci. Lett. 258 (1), 87–100.

Konhauser, K.O., Pecoits, E., Lalonde, S.V., Papineau, D., Nisbet, E.G., Barley, M.E., Arndt, N.T., Zahnle, K., Kamber, B.S., 2009. Oceanic nickel depletion and a methanogen famine before the Great Oxidation Event. Nature 458 (7239), 750–753.

Konhauser, K.O., Planavsky, N., Hardisty, D., Robbins, L., Warchola, T., Haugaard, R., Lalonde, S., Partin, C., Oonk, P., Tsikos, H., 2017a. Iron formations: A global record of Neoarchaean to Palaeoproterozoic environmental history. Earth Sci. Rev. 172, 140–177.

Konhauser, K.O., Robbins, L.J., Alessi, D.S., Flynn, S.L., Gingras, M.K., Martinez, R.E., Kappler, A., Swanner, E.D., Li, Y.-L., Crowe, S.A., Planavsky, N.J., Reinhard, C.T., Lalonde, S.V., 2017b. Phytoplankton contributions to the trace-element composition of Precambrian banded iron formations. GSA Bull. 130 (5–6), 941–951.

Krissansen-Totton, J., Arney Giada, N., Catling David, C., 2018. Constraining the climate and ocean pH of the early Earth with a geological carbon cycle model. Proc. Natl. Acad. Sci. 115 (16), 4105–4110.

Lechte, M.A., Wallace, M.W. and Hoffmann, K.-H., 2019. Glacio-marine iron formation deposition in a c. 700 Ma glaciated margin: insights from the Chuos Formation, Namibia. Geological Society, London, Special Publications, 475(1): 9-34.

Li, Z., Cole, D.B., Newby, S.M., Owens, J.D., Kendall, B., Reinhard, C.T., 2021. New constraints on mid-Proterozoic ocean redox from stable thallium isotope systematics of black shales. Geochim. Cosmochim. Acta 315, 185–206.

Li, Z., Konhauser, K.O., Zhou, Y., Adlakha, E., Button, M., Lazowski, C., Pecoits, E., Aubet, N.R., Lecumberri-Sanchez, P., Alessi, D.S. and Robbins, L.J., 2023. How does weathering influence geochemical proxies in Paleoproterozoic banded iron formations? A case study from outcrop samples of 2.46 Ga banded iron formation, Hamersley Basin, Western Australia. GSA Bulletin.

Li, J., Lu, Y., Shim, H., Deng, X., Lian, J., Jia, Z., Li, J., 2010. Use of the BCR sequential extraction procedure for the study of metal availability to plants. J. Environ. Monit. 12 (2), 466–471.

Lin, R., Stuckman, M., Howard, B.H., Bank, T.L., Roth, E.A., Macala, M.K., Lopano, C., Soong, Y., Granite, E.J., 2018. Application of sequential extraction and hydrothermal treatment for characterization and enrichment of rare earth elements from coal fly ash. Fuel 232, 124–133.

Liu, H., Pourret, O., Guo, H., Bonhoure, J., 2017. Rare earth elements sorption to iron oxyhydroxide: Model development and application to groundwater. Appl. Geochem. 87, 158–166.

Maynard, J.B., 2012. Geochemistry of sedimentary ore deposits. Springer Science & Business Media.

McConchie, D., 1987. The geology and geochemistry of the Joffre and Whaleback shale members of th Brockman iron formation. Western Australia, Precambrian iron-formations, pp. 541–597.

Migdisov, A., Williams-Jones, A.E., Brugger, J., Caporuscio, F.A., 2016. Hydrothermal transport, deposition, and fractionation of the REE: Experimental data and thermodynamic calculations. Chem. Geol. 439, 13–42.

Morris, R.C., 1993. Genetic modelling for banded iron-formation of the Hamersley Group, Pilbara Craton, Western Australia. Precambrian Research 60 (1), 243–286.

Nan, J., Tsang, M.-Y., Li, J., Köster, M., Henkel, S., Lin, F. and Yao, W., 2023. Postdepositional Behavior of Molybdenum in Deep Sediments and Implications for Paleoredox Reconstruction. Geophysical Research Letters, 50(21): e2023GL104706.

Ohmoto, H., Watanabe, Y., Yamaguchi, K.E., Naraoka, H., Haruna, M., Kakegawa, T., Hayashi, K.-i. and Kato, Y., 2006. Chemical and biological evolution of early Earth: Constraints from banded iron formations. In: S.E. Kesler and H. Ohmoto (Editors), Evolution of Early Earth's Atmosphere, Hydrosphere, and Biosphere - Constraints from Ore Deposits. Geological Society of America, pp. 0.

Oonk, P., Mason, P., Tsikos, H., Bau, M., 2018. Fraction-specific rare earth elements enable the reconstruction of primary seawater signatures from iron formations. Geochim. Cosmochim. Acta 238, 102–122.

Oonk, P.B.H., Tsikos, H., Mason, P.R.D., Henkel, S., Staubwasser, M., Fryer, L., Poulton, S.W., Williams, H.M., 2017. Fraction-specific controls on the trace element distribution in iron formations: Implications for trace metal stable isotope proxies. Chem. Geol. 474, 17–32.

Oonk, P.B.H., 2017. Fraction-specific geochemistry across the Asbestos Hills BIF of the Transvaal Supergroup, South Africa: implications for the origin of BIF and the history of atmospheric oxygen, Rhodes University.

Oyeyiola, A.O., Olayinka, K.O., Alo, B.I., 2011. Comparison of three sequential extraction protocols for the fractionation of potentially toxic metals in coastal sediments. Environ. Monit. Assess. 172 (1), 319–327.

Ozaki, K., Thompson, K.J., Simister, R.L., Crowe, S.A., Reinhard, C.T., 2019. Anoxygenic photosynthesis and the delayed oxygenation of Earth's atmosphere. Nat. Commun. 10 (1), 3026.

Panias, D., Taxiarchou, M., Paspaliaris, I., Kontopoulos, A., 1996. Mechanisms of dissolution of iron oxides in aqueous oxalic acid solutions. Hydrometall. 42 (2), 257–265.

Pecoits, E., Gingras, M., Barley, M., Kappler, A., Posth, N., Konhauser, K., 2009. Petrography and geochemistry of the Dales Gorge banded iron formation: Paragenetic sequence, source and implications for palaeo-ocean chemistry. Precambr. Res. 172 (1–2), 163–187.

Peng, Z., Wang, C., Tong, X., Zhang, L., Zhang, B., 2018. Element geochemistry and neodymium isotope systematics of the Neoarchean banded iron formations in the Qingyuan greenstone belt, North China Craton. Ore Geol. Rev. 102, 562–584.

Planavsky, N., Bekker, A., Rouxel, O.J., Kamber, B., Hofmann, A., Knudsen, A., Lyons, T. W., 2010. Rare Earth Element and yttrium compositions of Archean and Paleoproterozoic Fe formations revisited: New perspectives on the significance and mechanisms of deposition. Geochim. Cosmochim. Acta 74 (22), 6387–6405.

Poulton, S.W., Canfield, D.E., 2005. Development of a sequential extraction procedure for iron: implications for iron partitioning in continentally derived particulates. Chem. Geol. 214 (3–4), 209–221.

Pourmand, A., Dauphas, N., Ireland, T.J., 2012. A novel extraction chromatography and MC-ICP-MS technique for rapid analysis of REE, Sc and Y: Revising CI-chondrite and Post-Archean Australian Shale (PAAS) abundances. Chem. Geol. 291, 38–54.

Quinn, K.A., 2006. Influence of solution and surface chemistry on yttrium and rare earth element sorption. University of South Florida.

Rasmussen, B., Meier, D.B., Krapež, B., Muhling, J.R., 2013. Iron silicate microgranules as precursor sediments to 2.5-billion-year-old banded iron formations. Geology 41 (4), 435–438.

Rasmussen, B., Muhling, J.R., Suvorova, A., Krapež, B., 2017. Greenalite precipitation linked to the deposition of banded iron formations downslope from a late Archean carbonate platform. Precambr. Res. 290, 49–62.

Rasmussen, B., Muhling, J.R., Fischer, W.W., 2019. Evidence from laminated chert in banded iron formations for deposition by gravitational settling of iron-silicate muds. Geology 47 (2), 167–170.

Sampaio, G.M.S., Pufahl, P.K., Raye, U., Kyser, K.T., Abreu, A.T., Alkmim, A.R., Nalini, H.A., 2018. Influence of weathering and hydrothermal alteration on the REE and δ56Fe composition of iron formation, Cauê Formation, Iron Quadrangle, Brazil. Chem. Geol. 497, 27–40.

Schopf, J.W., Barghoorn Elso, S., 1967. Alga-Like Fossils from the Early Precambrian of South Africa. Science 156 (3774), 508–512.

Smrzka, D., Zwicker, J., Bach, W., Feng, D., Himmler, T., Chen, D., Peckmann, J., 2019. The behavior of trace elements in seawater, sedimentary pore water, and their incorporation into carbonate minerals: a review. Facies 65 (4), 41.

Spry, P.G., Marshall, B., Vokes, F.M., 2000. Metamorphosed and metamorphogenic ore deposits, 11. Society of Economic Geologists.

Stammeier, J.A., Hippler, D., Nebel, O., Leis, A., Grengg, C., Mittermayr, F., Kasemann, S. A., Dietzel, M., 2019. Radiogenic Sr and Stable C and O Isotopes Across Precambrian-Cambrian Transition in Marine Carbonatic Phosphorites of Malyi Karatau (Kazakhstan)—Implications for Paleo-environmental Change. Geochem. Geophys. Geosyst. 20 (1), 3–23.

Steinhoefel, G., Horn, I., von Blanckenburg, F., 2009. Micro-scale tracing of Fe and Si isotope signatures in banded iron formation using femtosecond laser ablation. Geochim. Cosmochim. Acta 73 (18), 5343–5360.

Sun, S.-S., McDonough, W.F., 1989. Chemical and isotopic systematics of oceanic basalts: implications for mantle composition and processes. Geol. Soc. Lond. Spec. Publ. 42 (1), 313–345.

Suter, D., Siffert, C., Sulzberger, B., Stumm, W., 1988. Catalytic dissoluion of iron(III) (hydr)oxides by oxalic acid in the presence of Fe(II). Naturwissenschaften 75 (11), 571–573.

Sylvestre, G., Evine Laure, N.T., Gus Djibril, K.N., Arlette, D.S., Cyriel, M., Timoléon, N., Jean Paul, N., 2017. A mixed seawater and hydrothermal origin of superior-type banded iron formation (BIF)-hosted Kouambo iron deposit, Palaeoproterozoic Nyong series, Southwestern Cameroon: Constraints from petrography and geochemistry. Ore Geol. Rev. 80, 860–875.

Tabata, H., Sekine, Y., Kanzaki, Y., Sugita, S., 2021. An experimental study of photo-oxidation of Fe(II): Implications for the formation of Fe(III) (hydro)oxides on early Mars and Earth. Geochim. Cosmochim. Acta 299, 35–51.

Takahashi, Y., Murata, M., Kimura, T., 2006. Interaction of Eu(III) ion and non-porous silica: Irreversible sorption of Eu(III) on silica and hydrolysis of silica promoted by Eu(III). J. Alloy. Compd. 408–412, 1246–1251.

Takematsu, N., 1979. Sorption of transition metals on manganese and iron oxides, and silicate minerals. J. Oceanogr. Soc. Jpn. 35 (1), 36–42.

Taxiarchou, M., Panias, D., Douni, I., Paspaliaris, I., Kontopoulos, A., 1997. Dissolution of hematite in acidic oxalate solutions. Hydrometall. 44 (3), 287–299.

Thibon, F., Blichert-Toft, J., Tsikos, H., Foden, J., Albalat, E., Albarede, F., 2019. Dynamics of oceanic iron prior to the Great Oxygenation Event. Earth Planet. Sci. Lett. 506, 360–370.

Thompson, K.J., Kenward, P.A., Bauer, K.W., Warchola, T., Gauger, T., Martinez, R., Simister, R.L., Michiels, C.C., Llirós, M., Reinhard, C.T., Kappler, A., Konhauser, K. O., Crowe, S.A., 2019. Photoferrotrophy, deposition of banded iron formations, and methane production in Archean oceans. Sci. Adv. 5 (11), eaav2869.

Thurston, P.C., Kamber, B.S., Whitehouse, M., 2012. Archean cherts in banded iron formation: Insight into Neoarchean ocean chemistry and depositional processes. Precambr. Res. 214–215, 227–257.

Van Kranendonk, M., Ivanic, T., 2009. A new lithostratigraphic scheme for the northeastern Murchison Domain. Yilgarn Craton. Geological Survey of Western Australia, Perth, pp. 35–53.

Van Kranendonk, M.J., Webb, G.E., Kamber, B.S., 2003. Geological and trace element evidence for a marine sedimentary environment of deposition and biogenicity of 3.45 Ga stromatolitic carbonates in the Pilbara Craton, and support for a reducing Archaean ocean. Geobiology 1 (2), 91–108.

Van Kranendonk, M.J., Ivanic, T.J., Wingate, M.T.D., Kirkland, C.L., Wyche, S., 2013. Long-lived, autochthonous development of the Archean Murchison Domain, and implications for Yilgarn Craton tectonics. Precambr. Res. 229, 49–92.

Viehmann, S., Bau, M., Hoffmann, J.E., Münker, C., 2015a. Geochemistry of the Krivoy Rog Banded Iron Formation, Ukraine, and the impact of peak episodes of increased global magmatic activity on the trace element composition of Precambrian seawater. Precambr. Res. 270, 165–180.

Viehmann, S., Bau, M., Smith, A.J.B., Beukes, N.J., Dantas, E.L., Bühn, B., 2015b. The reliability of ~2.9 Ga old Witwatersrand banded iron formations (South Africa) as archives for Mesoarchean seawater: Evidence from REE and Nd isotope systematics. J. Afr. Earth Sc. 111, 322–334.

Viehmann, S., Reitner, J., Tepe, N., Hohl, S.V., Van Kranendonk, M., Hofmann, T., Koeberl, C., Meister, P., 2020. Carbonates and cherts as archives of seawater chemistry and habitability on a carbonate platform 3.35 Ga ago: Insights from Sm/Nd dating and trace element analysis from the Strelley Pool Formation, Western Australia. Precambr. Res. 344, 105742.

Vieira, J.S., Botelho, C.M.S., Boaventura, R.A.R., 2009. Trace Metal Fractionation by the Sequential Extraction Method in Sediments from the Lis River (Portugal). Soil Sediment Contam. Int. J. 18 (1), 102–119.

Wallace, M.W., Hood, A.v., Shuster, A., Greig, A., Planavsky, N.J. and Reed, C.P., 2017. Oxygenation history of the Neoproterozoic to early Phanerozoic and the rise of land plants. Earth and Planetary Science Letters, 466: 12-19.

Walter, X., Picazo Mozo, A., Miracle, M., Vicente, E., Camacho, A., Aragno, M., Zopfi, J., 2014. Phototrophic Fe(II)-oxidation in the chemocline of a ferruginous meromictic lake. Front. Microbiol. 5, 713.

Wang, C., Zhang, L., Lan, C., Dai, Y., 2014. Petrology and geochemistry of the Wangjiazhuang banded iron formation and associated supracrustal rocks from the Wutai greenstone belt in the North China Craton: implications for their origin and tectonic setting. Precambr. Res. 255, 603–626.

Wang, C., Konhauser, K.O., Zhang, L., 2015. Depositional Environment of the Paleoproterozoic Yuanjiacun Banded Iron Formation in Shanxi Province. China. Economic Geology 110 (6), 1515–1539.

Wang, C., Robbins, L.J., Planavsky, N.J., Beukes, N.J., Patry, L.A., Lalonde, S.V., Lechte, M.A., Asael, D., Reinhard, C.T., Zhang, L., Konhauser, K.O., 2023. Archean to early Paleoproterozoic iron formations document a transition in iron oxidation mechanisms. Geochim. Cosmochim. Acta 343, 286–303.

Wen, X., De Carlo, E.H., Li, Y.H., 1997. Interelement relationships in ferromanganese crusts from the central Pacific ocean: Their implications for crust genesis. Mar. Geol. 136 (3), 277–297.

Wingate, M., Kirkland, C., Van Kranendonk, M., Wyche, S., 2013. 155569: Metarhyolite. Weld Range 1096, 4 pp.

Winter, B.L., Knauth, L.P., 1992. Stable isotope geochemistry of cherts and carbonates from the 2.0 Ga gunflint iron formation: implications for the depositional setting, and the effects of diagenesis and metamorphism. Precambr. Res. 59 (3), 283–313.

Zhang, K., Shields, G.A., 2022. Sedimentary Ce anomalies: Secular change and implications for paleoenvironmental evolution. Earth Sci. Rev. 229, 104015.

Zhong, S., Mucci, A., 1995. Partitioning of rare earth elements (REEs) between calcite and seawater solutions at 25°C and 1 atm, and high dissolved REE concentrations. Geochim. Cosmochim. Acta 59 (3), 443–453.